

CHALMERS



Experimental measurements of Jeffery orbits of microrods in microchannels

MSc Thesis in Complex Adaptive Systems

Staffan Ankardal

Department of Applied Physics
CHALMERS UNIVERSITY OF TECHNOLOGY
Gothenburg, Sweden 2014
MSc Thesis 2014

Abstract

Orientational motion of axisymmetric particles in shear flow is important in a number of scientific fields. It was first studied theoretically by Jeffery, who showed that an axisymmetric particle in shear flow follows one of infinitely many periodic orbits depending on the initial condition of the particle. Later theoretical studies by Yarin *et al.* suggested that asymmetric particles may follow periodic, quasi-periodic, or chaotic orbits depending only on the initial conditions. This thesis attempts to experimentally verify Yarin's predictions, using glass particles in a reversible Stokes flow in a microfluidic PDMS channel. An optical tweezer is used to control the initial conditions. An automatic tracking of the particles was developed, and a number of improvements were made compared to previous experiments by Einarsson *et al.* [1]. We study the effects of asymmetry on the particles, and the transition from periodic to quasi-periodic orbits for different initial conditions, and for different degrees of asymmetry of the particles. Some measurements show good agreement with theoretical predictions, but there are also unexplained behaviours when the flow is reversed. The measurements were made in collaboration with Alexander Laas [2].

Acknowledgements

I hereby wish to thank my supervisors Bernhard Mehlig and Dag Hanstorp for helping me through this journey. I want to thank girlfriend Callie Gibbons for supporting me through the work on this thesis and Alexander Laas for being a tireless and understanding co-worker. I want to thank all the contributors to the wealth of open source software which I have used to create everything from most of the software to more of the figures and of course this very report.

Staffan Ankardal, Göteborg Sweden March 21, 2014

Contents

1	Introduction	1
1.1	Introduction	1
1.2	Background	1
2	Theory	4
2.1	Fluid dynamics	4
2.1.1	Reynolds number	4
2.1.2	Stokes drag and Stokes' law	6
2.2	Euler angles and coordinate system	7
2.2.1	Triaxial particles	9
2.3	Jeffery orbits	9
2.3.1	Winding number	13
3	Method	17
I	Improvements of experimental setup	18
3.1	Experimental setup	19
3.1.1	List of equipment	23

3.2	Problems and improvements	23
3.2.1	Particles and channel	24
3.3	Automated tracking	27
3.3.1	Acquiring the image	28
3.3.2	Reducing noise	28
3.3.3	Contour detection and selection	29
3.3.4	Adjusting the camera velocity	30
3.3.5	Time considerations	30
3.4	Summary of improvements	31
II	Data analysis and results	33
4	Data analysis	34
4.1	Particle identification	34
4.2	Estimation of orientation	35
4.3	Width compensation	36
4.4	Removing tracking errors	38
4.5	Estimating the winding numbers	38
4.6	Matching data to theoretical orbits	40
5	Results	43
5.1	Measurements	44
5.1.1	Measurements of particle A	44
5.1.2	Measurements of particle B	47
5.2	Diagnostic plots	51
5.2.1	Reversals	54
5.3	Match to theoretical orbits	56
5.3.1	Particle A	56
5.3.2	Particle B	57

6 Discussion	61
6.1 Sinking	62
6.2 Reversals where the orbit changes	63
6.2.1 Possible expansion of the channel	63
6.3 Winding number matching	64
6.4 Unexplained behaviours	65
6.5 Width compensation	66
6.6 Goodness of fit	66
6.7 Automated tracking	69
7 Conclusion	71

1

Introduction

1.1 Introduction

My goal in this thesis is to study and better understand the dynamics of ellipsoidal particles in shear flows. The thesis is a continuation of two previous MSc theses [3, 4]. The methodology is to experimentally measure the orientational dynamics of μm -sized glass particles in a shear flow, then compare the results to results from theoretical models.

In the first part of the thesis, I describe the improvements that were made to the experimental setup, in particular an automated tracking system. In the second part of the thesis, the measurements and their analysis is discussed. But before discussing either of these subjects more in depth some background is needed.

1.2 Background

Understanding the orientational dynamics of particles in flow might appear somewhat esoteric to someone unfamiliar with the topic, but it is used in a wide variety of fields. In medical applications understanding the dynamics of ellipsoidal particles such as bacteria can be relevant to a detailed

1.2. BACKGROUND

understanding of their interactions with cells and other bodies [5]. In geology the rotational dynamics of mineral grains in magma flows determines rock structures which form after the magma cools [6].

One of the first papers to show the importance of understanding particle dynamics in flow was by Einstein in 1905 [7]. He showed how the rotation of spherical particles suspended in a liquid increases the viscosity of the liquid. Jeffery in his 1922 paper [8] extended these results to ellipsoidal particles and for systems where inertial effects could be discarded he derived equations for the orientational dynamics of the particles. He also solved the equations for axisymmetric particles and found their motion to be periodic and depending only on the initial condition of the particle.

Investigation of triaxial particles was started by Gierszewski & Chaffey [9] and was continued by Hinch & Leal [10] and more recently by Yarin *et al.* [11]. The dynamics Jeffery had found for axisymmetric particles was periodic, but it was shown by Hinch & Leal that for triaxial particles some orbits could be doubly periodic, in other words exhibiting two separate independent periods. This behaviour is referred to as *quasi-periodic* in this thesis.

Yarin *et al.* used numerical simulations to generate a surface of section [12] for ellipsoidal particles with different shapes. They showed that not only were there doubly periodic or quasi-periodic orbits but when the ellipsoids had sufficiently different minor and median axes there could be chaotic orbits. In these orbits the particles rotate periodically perpendicular to the flow but the orientation of the particles in the flow changes unpredictably over longer time scales.

Several other surfaces of section were produced by Johansson [3] using the same method as Yarin *et al.* It was shown that even small asymmetries of the order of 1% lead to quasi-periodic motion for some initial conditions.

Attempts to experimentally verify the theoretical results of Jeffery were initially performed by Goldsmith and Mason in 1962 [13] who used flow in a glass pipe to observe the rotation rate of particles of several different shapes. They confirmed that the rotation rate matched well with that predicted from Jeffery orbits but they did not study the actual orbits. Since then most experimental research, such that as by Harlen and Koch [14], has focused on how dilute suspensions of particles affect the properties of a liquid. Only tangential efforts such as by Tolga [5] were concerned with

1.2. BACKGROUND

the Jeffery orbits. An excellent summary of both theoretical and experimental results was written by Petrie [15] in 1999.

Dedicated experiments to measure the actual Jeffery orbits in angular components and verify the orientational dynamics were performed by Einarsson *et al.* [1]. They studied the rotational dynamics of $\sim 20\text{-}30\mu\text{m}$ long and $\sim 1\mu\text{m}$ wide polymer particles in a microfluidic channel. The orientational motion of some particles were shown to be qualitatively similar to some Jeffery orbits. These particles also very closely retraced their motion when reversing the flow implying that no significant amount of noise had disturbed their orientational motion nor had there been any inertial effects. The vast majority of particles were asymmetric to the degree that their orbits were chaotic or highly quasi-periodic. No particular particle could also be shown to exhibit both quasi-periodic and periodic motion. Moreover the width and length of particles varied greatly and could not be measured accurately.

The goal of this thesis is to improve the setup from Johansson [3] and Einarsson *et al.* [1] in order to experimentally verify the results of Yarin *et al.* [11] and Hinch, Leal [10]. The aim is to show that the same particle may exhibit different types of motion for different initial conditions: Periodic motion, quasi-periodic motion and chaotic motion. Furthermore that particles with different asymmetries may show different motion for the same initial conditions. To this end we observe the orientation of a μm length particle in a creeping shear flow. Using μm sized particles guarantee that there are no inertial effects and the particles are also small enough to be controlled by optical tweezers. The flow is shown to be creeping by demonstrating that the particle dynamics revert as the flow is reversed. The results are compared to theoretical predictions for different initial conditions and asymmetries.

2

Theory

In order to better understand the results and discussions in this thesis, basic knowledge of fluid mechanics and image analysis is needed. This is given in this chapter along with a more detailed discussion of Jeffery orbits in particular.

Since the main focus of this thesis is experimental, the theory background is only briefly summarized. A more inquisitive reader is recommended to read Einarssons licentiate thesis [16] which goes into greater detail concerning most of the topics covered in this chapter.

2.1 Fluid dynamics

In order to understand the motivations for, as well as the limitations and the behaviour of, the experiment we need to know about a few key concepts in fluid mechanics.

2.1.1 Reynolds number

The Reynolds number (Re) is a dimensionless number describing the ratio of the strength of inertial forces to the strength viscous forces in a flow. Roughly speaking one can think of viscous forces as acting to keep adjacent fluid elements moving in the same direction whereas inertial forces act to

2.1. FLUID DYNAMICS

prevent any change in the motion of a fluid element. For a flow the Reynolds number is defined as [17]

$$\text{Re} = \frac{UW\rho}{\mu} \quad (2.1)$$

where U is the characteristic velocity of the flow, W is its characteristic length scale, ρ is the density of the fluid, and μ is its dynamic viscosity. The Reynolds number is used to characterize the regime of the flow. There are two primary regimes

1. Laminar regime, where viscous forces dominate over inertial forces.
2. Turbulent regime where inertial forces dominate.

A simple visual characterization of the flow types can be seen in Figure 2.1.

Flow with $\text{Re} \ll 1$ is referred to as *Stokes flow*. In this regime we can ignore inertial forces completely. The flow is guaranteed to be laminar, and it is also time reversible. This means any dynamics of the fluid are retraced when the flow is reversed, as if time was reversed. [18]

Particles in Stokes flow are also time reversible if they have a particle Reynolds number $\text{Re}_p \ll$

1. The particle Reynolds number is defined as [16]

$$\text{Re}_p = \frac{u_p L \rho}{\mu}. \quad (2.2)$$

Here u_p is the typical flow speed relative to the particle surface, L is the characteristic size of the particle, ρ is the density of the fluid and μ is the dynamic viscosity of the fluid.

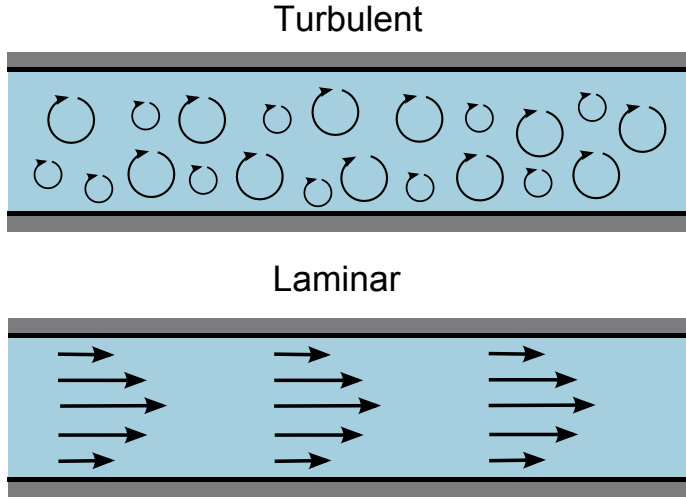


Figure 2.1: This shows the principal difference between laminar and turbulent flow.

2.1.2 Stokes drag and Stokes' law

For $\text{Re} = 0$ the drag force F_D exerted by a fluid on a spherical particle is found using Stokes's law [19]

$$F_D = 6\pi\mu Rv. \quad (2.3)$$

Here v is the velocity of the sphere relative to the fluid, μ is the dynamic viscosity, and R is the radius of the sphere. This can be used to find the terminal velocity of a sphere sinking in a liquid by equating the gravitational force F_G acting on the sphere with the drag force from eq 2.3. F_G is calculated as

$$F_G = \Delta\rho g \frac{4\pi R^3}{3}, \quad (2.4)$$

where $\Delta\rho$ is the difference in density between the fluid and the sphere and g is the specific gravity. By equation eq (2.3) and eq (2.4) we find that the terminal velocity of a sinking (or floating) sphere is

$$v_s = \frac{2}{9} \frac{\Delta\rho}{\mu} g R^2. \quad (2.5)$$

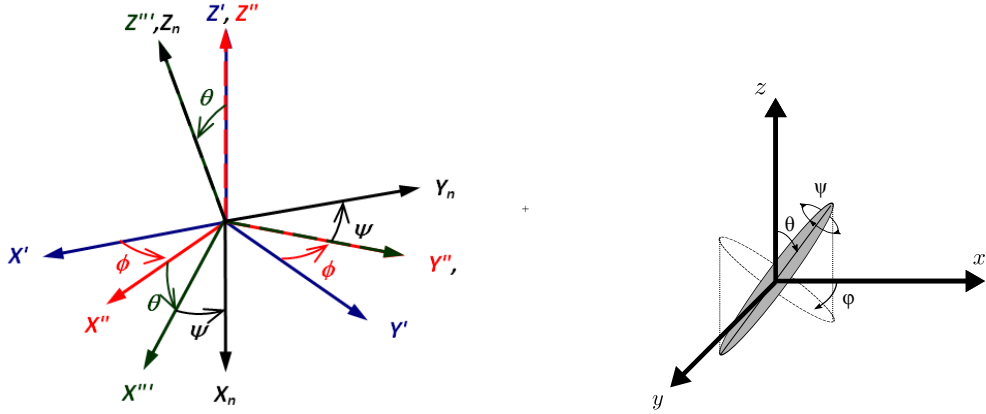
This is not immediately applicable to cylindrical particles but serves as a first order approximation.

2.2 Euler angles and coordinate system

When describing rotating particles it is common to use the so-called Euler angles (ϕ, θ, ψ) . A formal definition is given by Diebel [20] but for the purposes of this thesis we describe them as a transformation. We start with a stationary right-hand coordinate system $\{x,y,z\}$ with the x -axis along the length of the channel, the z -axis along the width of the channel, and the y -axis along depth. We define the Euler angles as the transformation from the channel coordinate system to the coordinate system attached to our particle $\{x',y',z'\}$. This transformation is performed in three steps by using an intermediate axis T.

- Rotate the x - y plane ϕ radians about the z -axis.
- Denote the shifted x -axis T and rotate the z - y' plane θ radians around the T -axis
- Denote the shifted z -axis z' and rotate the x' - y' plane ψ radians around the z' axis.

This procedure is illustrated in Figure 2.2a where each prime marks one additional step of rotation to the coordinate system. Figure 2.2b shows the Euler angles for a triaxial particle from a point of view similar to that of the experiment where the x - z plane is the field of view. Note that although ψ has an impact on the particle dynamics, we cannot observe it in our experiment as the particles are too symmetric around that axis, as is shown in section 3.2.1



(a) A general illustration of the Euler angles (b) The Euler angles as used in our experiment

Figure 2.2: Figure (a): The Euler angles illustrated using a series of coordinate rotations. Figure (b): The Euler angles illustrated using an ellipsoid. This alternate visualization shows the angles with a point of view similar to that of the camera in the experiment.

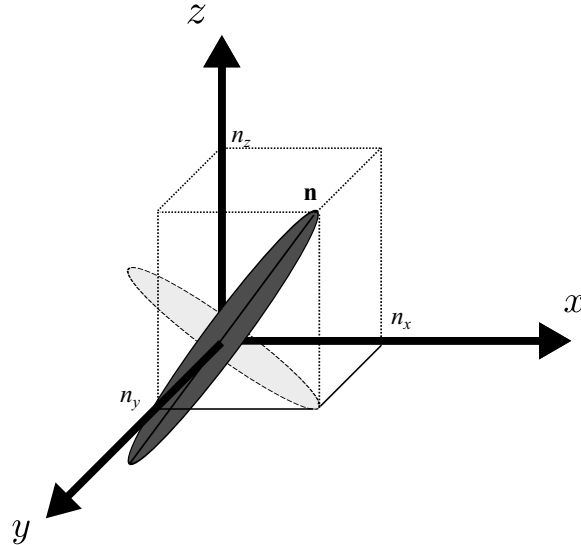


Figure 2.3: The unit vector \mathbf{n} and its components n_x , n_y and n_z . The vector \mathbf{n} is a unit vector, $|\mathbf{n}| = 1$.

The conversion from (ϕ, θ, ψ) to the unit vector $\mathbf{n} = (n_x, n_y, n_z)$ is given by

$$n_x = \sin(\theta) \cos(\psi), \quad (2.6a)$$

$$n_y = \sin(\theta) \sin(\psi), \quad (2.6b)$$

$$n_z = \cos(\theta). \quad (2.6c)$$

In particular n_z and $\cos(\theta)$ are used interchangeably.

2.2.1 Triaxial particles

A triaxial particle is an ellipsoidal particle that has a distinct radius around the x -axis, y -axis and z -axis. In other words it has distinct length, width and height. We refer to these lengths as a_1, a_2, a_3 with $a_1 > a_2 > a_3$.

When discussing triaxial particles that are close to being axisymmetric of the form $a_1 \gg a_2 \approx a_3$, it is convenient to introduce the particle asymmetry ϵ defined as

$$\epsilon = \frac{a_2}{a_3} - 1, \quad (2.7)$$

and the aspect ratio λ given by

$$\lambda = \frac{a_1}{a_2}. \quad (2.8)$$

These parameters are as used by among others Yarin *et al.* [11] to characterize the particles used in simulations and experiments.

2.3 Jeffery orbits

The Jeffery orbits describe the orientational motion of an ellipsoidal particle in Stokes flow. The general equations of motion for any ellipsoid in shear flow were found by Jeffery [8] who also solved these equations of motion for axisymmetric ($a_1 \neq a_2 = a_3$) ellipsoidal particles. Solutions for

asymmetric particles were found numerically by Yarin *et al.* [11] who also rewrote the equations in a different but equivalent form. The equations of rotational motion for a triaxial particle in shear flow are in the form of Yarin *et al.*

$$\frac{d\theta}{dt} = (g_2 \sin \psi + g_3 \cos \psi) \sin \theta, \quad (2.9a)$$

$$\frac{d\phi}{dt} = \frac{1}{2} + g_3 \sin \psi - g_2 \cos \psi, \quad (2.9b)$$

$$\frac{d\psi}{dt} = g_1 + (g_2 \cos \psi - g_3 \sin \psi) \cos \theta. \quad (2.9c)$$

$$(2.9d)$$

The functions g_i are defined as

$$g_1 = \frac{a_2^2 - a_3^2}{2(a_2^2 + a_3^2)} \left(-\frac{1}{2}(\cos^2 \theta + 1) \sin 2\phi \sin 2\psi + \cos \theta \cos 2\phi \cos 2\psi \right), \quad (2.10a)$$

$$g_2 = \frac{a_3^2 - a_1^2}{2(a_1^2 + a_3^2)} \left(-\cos \theta \sin 2\phi \sin \psi + \cos 2\phi \cos \psi \right), \quad (2.10b)$$

$$g_3 = \frac{a_1^2 - a_2^2}{2(a_1^2 + a_2^2)} \left(\cos \theta \sin 2\phi \cos \psi + \cos 2\phi \sin \psi \right). \quad (2.10c)$$

Here (ϕ, θ, ψ) are the Euler angles seen in Figure 2.2a.

Note that the eq. (2.9) uses the coordinate system from Yarin *et al.*[11] which differ from the one used in this thesis, details are discussed in Johansson [3]. Numerical solutions for three different initial conditions for an asymmetric particle are shown in Figure 2.4b.

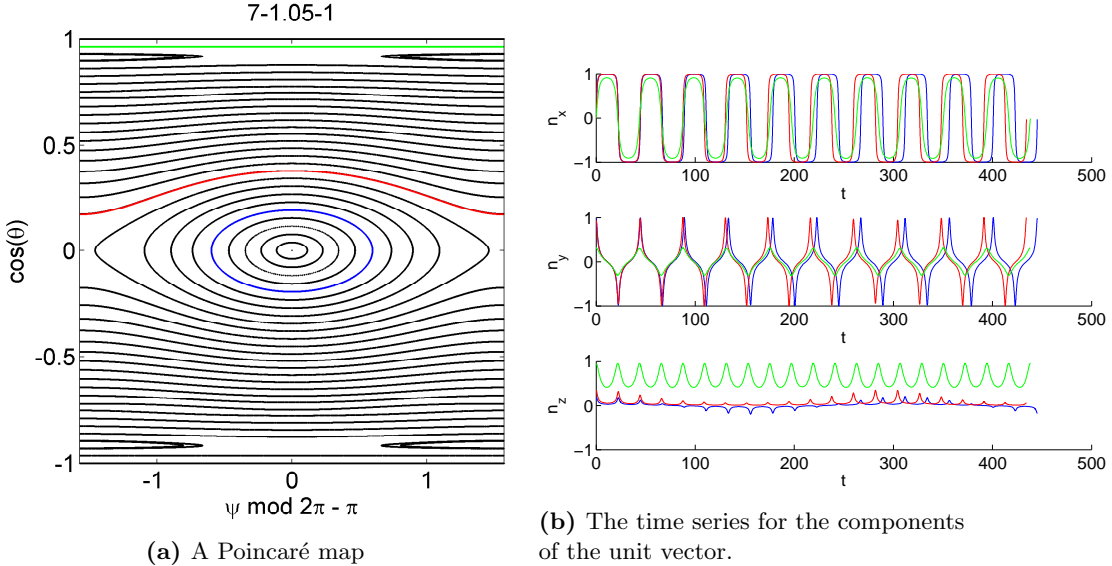


Figure 2.4: A Poincaré map and three different orbits for a simulated particle with $\lambda = 7$ and $\epsilon = 0.05$. The three orbits highlight the three different kinds of motion, the quasi-periodic sign changing orbit in blue, the quasi-periodic sign preserving orbit in red and the periodic orbit in green. The motion in n_x and n_y look qualitatively similar but differ in amplitude for the different orbits, n_z shows three different types of behaviour.

Looking at Figure 2.4b we see that n_x and n_y are periodic, corresponding to periodic rotation around the z -axis. We refer to these rotations as flips. The period η of n_x and n_y is for an axisymmetric particle [8]

$$\eta = 2\pi \left(\lambda + \frac{1}{\lambda} \right) \frac{1}{\kappa}, \quad (2.11)$$

where κ is the shear rate.

The time evolution of θ and ψ for different initial conditions can be plotted in a Poincaré map, also known as a Surface-of-Section (S.O.S.) [21]. This plots the ψ and θ coordinates each time $\phi = 0$. The successive points on the Poincaré map for each initial condition move and explore certain regions of the surface of section. This region is referred to as the *orbit*.

For a particle with an asymmetry ϵ in the range $[0.01 - 0.05]$ there are three classes of orbits, depending on the initial condition θ_0 .

2.3. JEFFERY ORBITS

1. **Periodic:** $|\theta_0| \approx 1$ in which there is little variation and the particle is largely periodic with fluctuations too small to measure.
2. **Quasi-periodic sign preserving:** For $|\theta_0| > \theta_b$ the amplitude of $\cos(\theta)$ changes noticeably but does not change sign. Here θ_b is a breaking point that changes for different ϵ .
3. **Quasi-periodic sign changing:** For small $|\theta_0| < \theta_b$ the amplitude of $\cos(\theta)$ changes noticeably and changes sign.

Simulations of these three different types of orbits for a particle with $\lambda = 7$ and $\epsilon = 0.05$ are illustrated in Figure 2.4. Figure 2.4 shows the orbits on the S.O.S. and Figure 2.4b shows the components of \mathbf{n} as a function of time. We can see that while n_x and n_y are periodic, albeit with different amplitudes, the behaviour of n_z is significantly different for the different orbits. The $n_z \approx 1$ orbit shown in green is constant on the S.O.S and is simply periodic over time. The sign preserving quasi-periodic orbit in red is bent on the S.O.S. We can see in the time series that it is doubly periodic as it peaks with a fixed period but the amplitude of the peaks vary periodically themselves. The sign changing quasi-periodic orbit in blue also peaks periodically with varying peak amplitude but these also change sign, again with a fixed period.

For larger asymmetries $\epsilon > 0.05$ there are chaotic orbits that explore a larger region of the S.O.S. The simulations used do not have long enough time scales for the chaotic orbits to 'fill' the regions in the way that quasi-periodic or periodic orbits fill the one dimensional regions that define their orbits. This results in the chaotic orbits appearing as a 'sea' of dots instead of filled lines or areas. Chaotic orbits can be seen around the quasi-periodic sign changing orbits in Figure 2.5d.

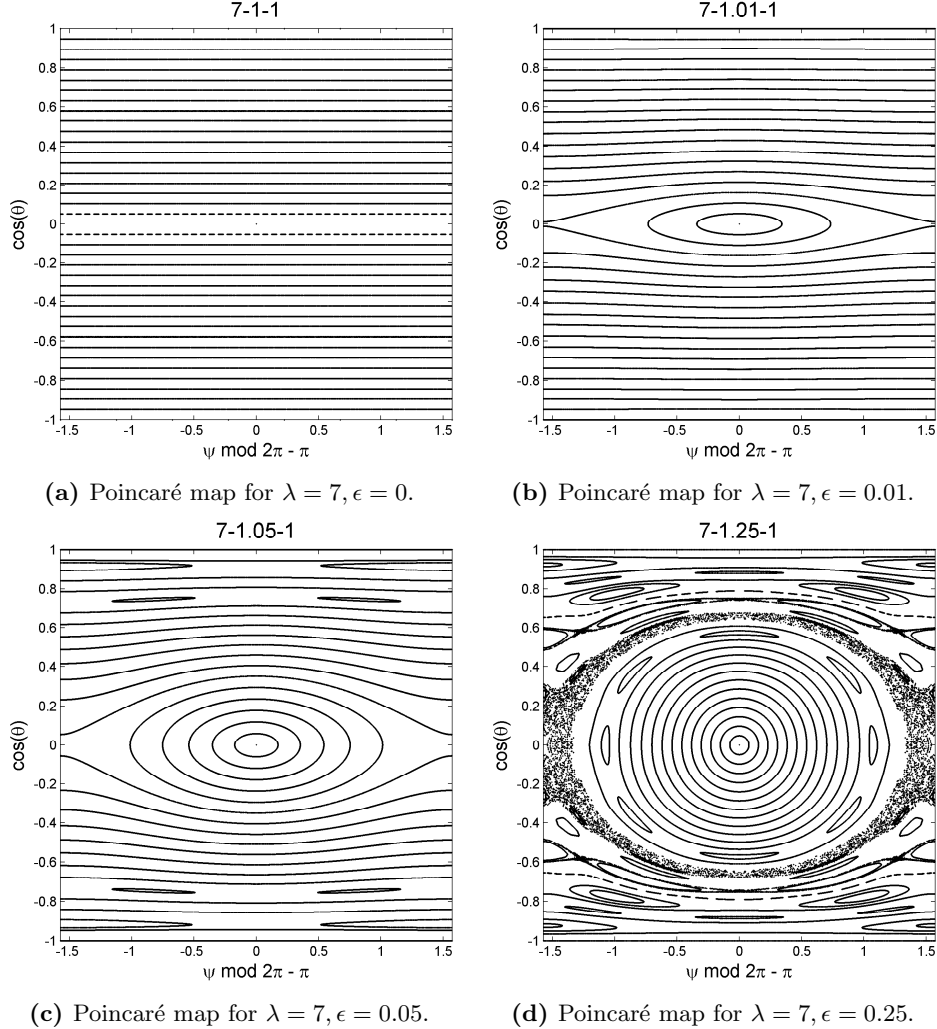


Figure 2.5: Four Poincaré maps for different ϵ . Already at $\epsilon = 0.01$ there are noticeably quasi-periodic orbits around the centre at $\cos(\theta) \approx \psi \approx 0$ but it is also a significantly larger region for $\epsilon = 0.05$. For $\epsilon = 0.25$ we can see chaotic orbits surrounding the circular orbits in the centre that appear as a 'sea' of dots.

2.3.1 Winding number

The quasi-periodic orbits are also referred to as doubly-periodic [11]. They are called doubly-periodic to emphasize the fact that the amplitude of a short period θ_2 also varies periodically with a longer period θ_1 . The ratio between the two periods is referred to as the winding number

ω referring to the winding around a unit torus. The shorter period θ_2 corresponds to rotations around the small cross section of the unit torus and the longer period θ_1 corresponds to rotations around the large circumference of the torus. The winding number is the fraction of these periods, as is shown in Figure 2.6.

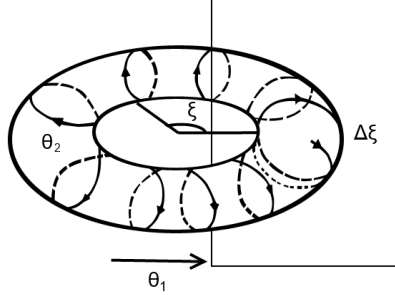


Figure 2.6: Winding around a unit torus with period θ_1 around the large circumference and θ_2 around the small cross section. The offset after one rotation around the large circumference θ_1/θ_2 is called the winding number. This figure idea was taken from Schuster [22]

The winding number is defined as [22]

$$\omega_{def} = \lim_{n \rightarrow \infty} \frac{f^n(\xi) - \xi_0}{n}. \quad (2.12)$$

Here ξ is the angle around the large circumference of the torus and $f^n(\xi)$ is the shift caused in n rotations around the smaller axis. Applying this to our double-periodic orbits ξ is the angle with period θ_1 and n is the number of flips with period θ_2 . Since we cannot measure ξ I consider it more comprehensible to consider the inverse winding number: the number of flips necessary to complete one period of ξ . This can be measured as is shown in Figure 2.7. If we measure over several θ_1 peaks the average winding number approximates the real one. We refer to the this inverse winding number as ω and it is given by

$$\omega = \frac{\theta_1}{\theta_2}. \quad (2.13)$$

The winding number of the quasi-periodic sign preserving orbit from Figure 2.4 and the way we

approximate θ_1 (and thereby ω) is illustrated in Figure 2.7.

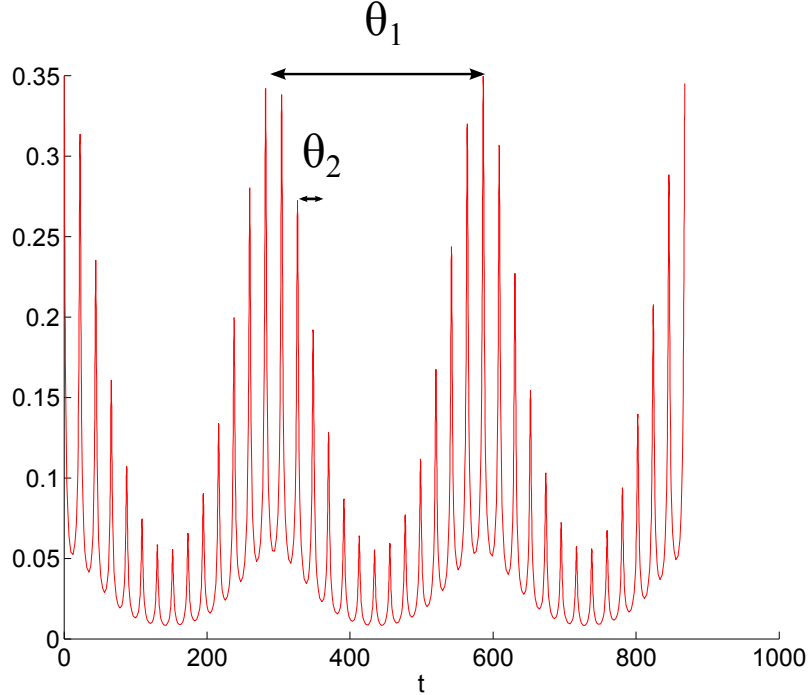


Figure 2.7: The quasi-periodic sign preserving orbit from Figure 2.4b over a longer time, highlighting the short period θ_2 which is simply the period of ϕ and the longer period θ_1 . We find the inverse winding number as the ratio between the longer and shorter periods.

The winding number is the same for any point along a quasi-periodic orbit on a Poincaré map but it is different for different orbits as well as for different asymmetries. The winding numbers for orbits along $\psi = 0$ for $\epsilon = \{0.01, 0.05, 0.10\}$ can be seen in Figure 2.8. The difference in winding number between the different ϵ for the sign changing orbits are almost a factor 2. This means that if we can measure the winding number for a sign changing orbit it allows us to approximate the asymmetry of the particle even though the variation in n_z are identical. Without looking at the winding number we cannot determine if a particle with an orbit close to $n_z = 0$ and small variations in amplitude is close to symmetric or not.

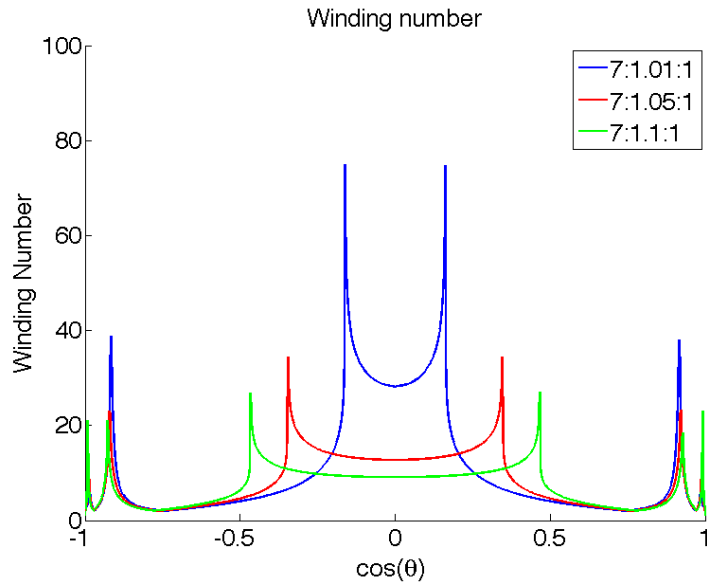


Figure 2.8: The winding number for $\psi_0 = 0$ and $\lambda = 7$ as a function of $\cos(\theta_0)$ for three different asymmetries, $\epsilon = 0.01$, $\epsilon = 0.05$ and $\epsilon = 0.10$. The sharp edge that occurs at different points for the different asymmetries, but centred around zero, is where the sign changing orbits end and sign preserving orbits begin, denoted by θ_b . We see that a lower asymmetry leads to a sharper difference between the sign changing and the sign preserving orbits and that higher asymmetry in general leads to lower winding numbers on average.

3

Method

Part I

Improvements of experimental setup

3.1. EXPERIMENTAL SETUP

In order to get accurate measurements of the Jeffery orbits we need a carefully designed experimental setup. The experimental setup used in this thesis is an iteration of the one used by Einarsson *et al.* [1], Johansson [3], and Mishra *et al.* [23]. In this chapter we describe the setup and why it is designed the way it is. In particular we describe a tracking algorithm that was implemented to make gathering data easier. We also discuss the improvements over previous iterations, as well as new problems that have arisen from the changes we made to the experimental setup.

3.1 Experimental setup

The orientational motion of μm -sized particles suspended in a liquid was investigated by pumping the liquid through a microfluidic channel using a syringe pump. The channel is placed on a moveable stage on top of a microscope. A particle is tracked by moving the stage to match the center of mass velocity of the particle in the channel, and thus keep the particle stationary in the field of view of the microscope. Connected to the microscope is a CCD camera recording the tracking as movies which are saved and analysed.

When the tracked particle gets within 10 mm of the inlets on the channel, the flow is reversed. If the particle retraces its motion when the flow is reversed we know that no noise has disturbed the motion and that the flow is Stokes flow, as discussed in Section 2.1. In order to reduce the sudden impact of the pressure difference caused by the flow reversal, the reversals are performed in several steps. At the start of a reversal, the infusion/withdrawal rate is reduced by 50% for 10 seconds, then stopped completely for 10 seconds. After this the pump resumes in the reverse direction at 50% of the normal flow rate for another 10 seconds before resuming at full speed.

The movies are analyzed as described in Section 4. We refer to the trajectory of the orientation vector **n** for a particle along one length of the channel a **stretch**, and a series of stretches for a single particle a **measurement**. A sketch of the experimental setup can be seen in Figure 3.1, and a photograph of the actual setup in Figure 3.2.

Between measurements, optical tweezers constructed by A. Laas were used to change the orientation of the particle. For details on optical tweezers see the introductory guide from Stanford [24],

3.1. EXPERIMENTAL SETUP

or Laas thesis [2].

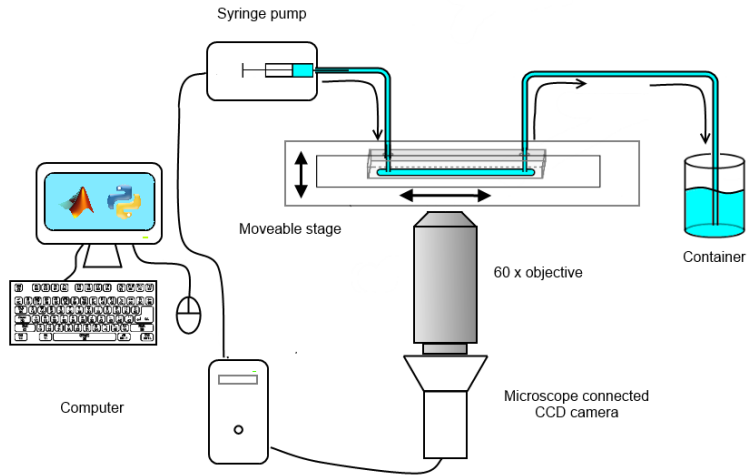


Figure 3.1: Sketch of the set up. The computer-controlled stage moves over the microscope. The pump reverses when the tracked particle gets close to the inlets of the channel. A CCD camera connected to the microscope records the dynamics of the particle as movies. Not pictured is the optical tweezer constructed by Laas [2] used to control the initial conditions of the particle between measurements.

3.1. EXPERIMENTAL SETUP

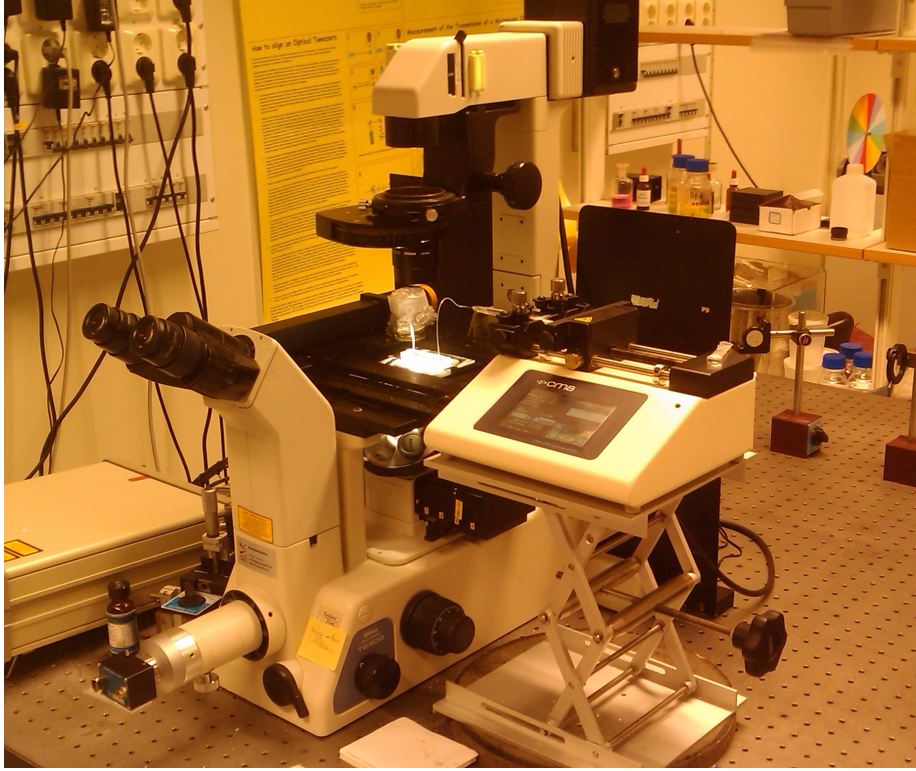


Figure 3.2: Overview of the set up. The microscope to the left and the syringe pump to the right. In the center is the channel and the outlet container is seen behind it. The CCD camera is mounted on the left side of the microscope and cannot be seen in this picture.

The microfluidic channel is 40 mm long, 2.5 mm wide and approximately 150 μm deep. The channel is made from Polydimethylsiloxane (PDMS) and plasma bonded to a microscope slide. A more detailed description of the process can be found from the Center for Computer Integrated Systems for Microscopy and Manipulation [25]. This material and procedure is chosen so that a channel that gets filled with dirt or breaks can cheaply and easily be replaced. Dirt in this case refers primarily to bubbles and to particles that stick to the glass or the PDMS. PDMS is non-reactive which means surface effects and other interactions with the particles are not a concern. PDMS is also highly transparent which means the light from the microscope illuminator won't be blocked or distorted before hitting the particles. A sketch of the channel can be seen in Figure 3.3a, and a photograph of an actual channel in Figure 3.3b.

3.1. EXPERIMENTAL SETUP

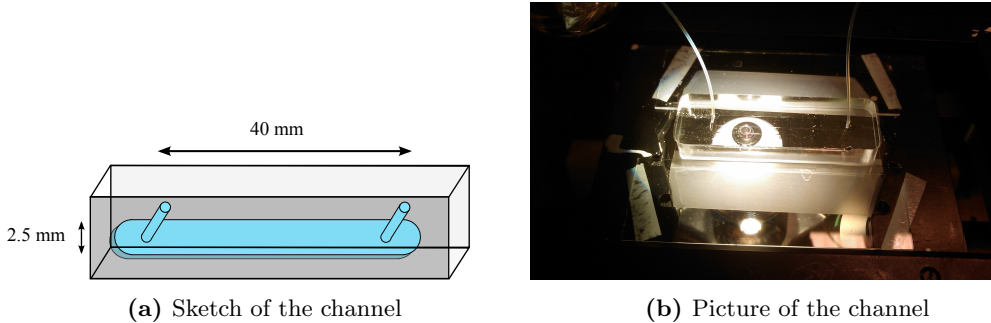


Figure 3.3: A sketch of the channel as well as a picture of the channel as it is set up during a measurement. The channel is only $150\mu\text{m}$ deep, but the PDMS surrounding it is around 15 mm to try and prevent the channel from expanding and contracting too much.

In order to find the maximum flow speed of the channel, we need to know the flow profile. Using the software employed by Johansson [3] which in turn is using results from Zheng [26], we solve the Poisson equation in a rectangular channel to obtain the flow profile. The solution for our channel measurements can be seen in Figure 3.4. Integrating the flow profile over the entire surface gives an effective flow area, essentially how large the channel 'actually' is. Using the flow profile from Figure 3.4 we find that the effective flow area is 0.14 mm^2 . With a pump rate of $7.5\mu\text{l}/\text{minute}$ we get a maximum speed of $v_{max}=0.90\text{ mm/s}$ for the liquid.

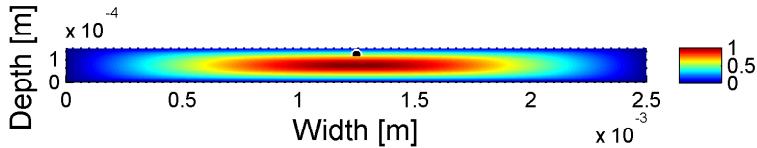


Figure 3.4: The theoretical estimation of the flow profile. Image generated with software from Johansson [3], used with permission.

We need to confirm that the flow is Stokes' flow and thus has no inertial effects. We can calculate the maximum Reynolds number using eq 2.1. Using the $3\mu\text{m}$ length of the particles as our characteristic length, and our maximum flow speed v_{max} :

$$\text{Re} = \frac{UW\rho}{\mu} \leq \frac{9.0 \cdot 10^{-4} \cdot 3 \cdot 10^{-3} 2.5}{24 \cdot 10^{-3}} \approx 2.78 \cdot 10^{-6} \ll 1. \quad (3.1)$$

3.2. PROBLEMS AND IMPROVEMENTS

This satisfies the conditions of validity for the Jeffery equations.

3.1.1 List of equipment

The equipment used during the experiment is as follows

- Leica DFC350 FX digital camera
- Nikon Eclipse TE 300 microscope
- Nikon 60x water immersion objective
- Märzhäuser Wetzlar 'LStep-eco' step engine
- CMA 4004 syringe pump
- Ytterbium fiber laser

3.2 Problems and improvements

As mentioned above this thesis is a continuation of previous work [1, 3, 23]. There were a number of problems that needed to be solved in order to improve the results. They can be summarized as:

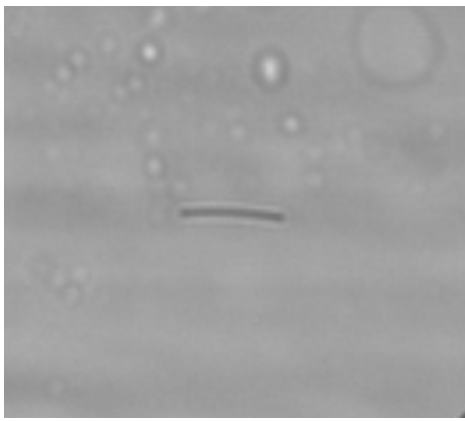
1. Particles

- Very few particles used in previous experiments were sufficiently symmetric to have periodic orbits or even quasi-periodic orbits. Most were visibly bent or uneven: see Figure 3.5
- The average aspect ratio of the particles was high which meant there were few flips along a stretch.
- The width of the particles was highly irregular and the resolution of the microscope did not allow for accurate measurements of it. This meant it was difficult to accurately estimate the aspect ratio.
- The particles could not be trapped with an optical tweezers due to low transmittance.

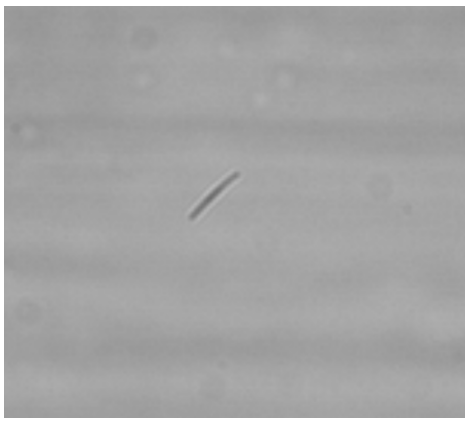
3.2. PROBLEMS AND IMPROVEMENTS

2. The PDMS in the channel was jagged which gave rise to noise unless the focus was in a very narrow band.
3. Manual tracking of particles was time consuming.
4. Bubbles were difficult to avoid when setting up the experiment.

3.2.1 Particles and channel



(a) Particle 13 from July 2012



(b) Particle 22 from July 2012

Figure 3.5: Two typical particles from the previous setup. Note that these particles are selected for being among the most symmetric in the sample and yet they are noticeably bent.

In order to solve the issues with the polymer particles, they were replaced with glass particles from Nippon Glass, Japan [27].

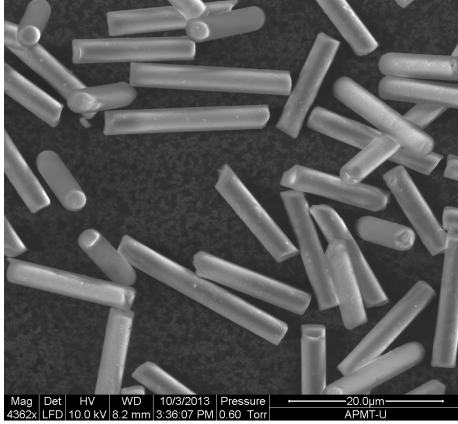
These new particles are made from LCD spacing rods that are broken into pieces. This means that they are essentially broken cylinders with very homogeneous widths but some variation in length. Two different batches of particles were used, one with a $3\mu m$ diameter and one batch with $5\mu m$ diameter. All the measurements presented in this thesis are using the $3\mu m$ width particles. This is primarily as they were more easily controlled with the optical tweezers and because they sink or float more slowly.

The symmetries of the particles were investigated with help from Stefan Gustafsson by taking images with an ESEM (Environmental Scanning Electron Microscope) shown in Figure 3.6. We see

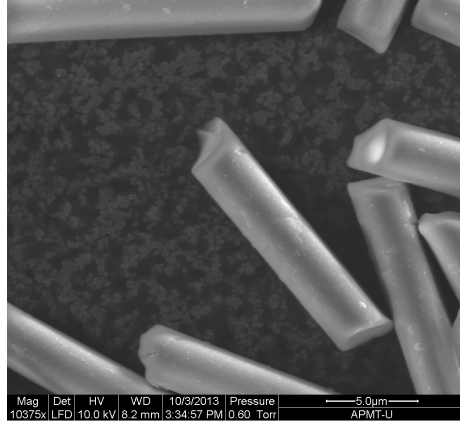
3.2. PROBLEMS AND IMPROVEMENTS

that the particles are uniformly smooth along the sides but have varyingly jagged edges causing different degrees of asymmetry.

Figure 3.7b shows a particle along the main axis. We see that it is a circular shape with no discernible deformation or asymmetry whereas Figure 3.6 shows the jagged edges of several particles.



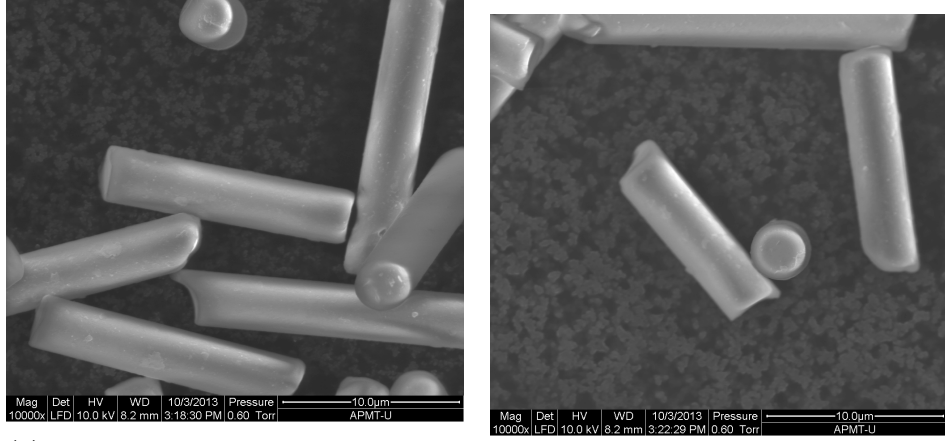
(a) A detailed view
of a number of particles.



(b) The jagged edge of a particle
in detail.

Figure 3.6: Pictures of the glass particles that were used. Their width is uniform and there is a noticeable variation in asymmetry. Some particles show very clearly jagged edges while other appear very smooth. This suggests that they have quite different ϵ , therefore exhibiting quite different behaviour. Obtained with the help of Stefan Gustafsson

3.2. PROBLEMS AND IMPROVEMENTS



(a) What appears to be a highly symmetric particle.

(b) A top down view of a particle.

Figure 3.7: Pictures highlighting the roundness of the particles as well as the apparent symmetry of some particles. Obtained with the help of Stefan Gustafsson

Figure 3.7b and 3.7a are the same as can be seen in Laas [2] Figure 5.2(c) and 5.2(b) respectively.

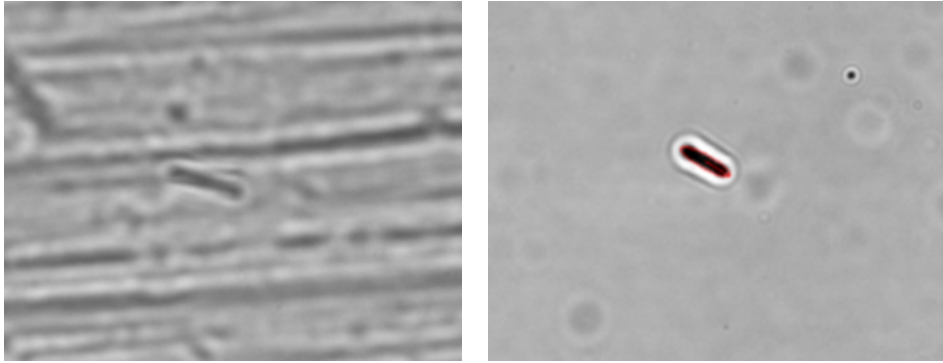
The particles satisfy the symmetry conditions but are made of glass with a density of approximately 2.57 g/cm^3 at 20°C . This is significantly higher than that of water with a density of 1 g/cm^3 at 20°C and glycerol with a density of 1.5 g/cm^3 . In order to keep the particles buoyant the water soluble Sodium metatungstate is added to the liquid. Sodium metatungstate dissolved in water has a density of 2.94 g/cm^3 at 20°C when fully saturated. To increase the viscosity of the liquid around 8% glycerol is added and the liquid was measured using a MCR 302 rheometer to have a dynamic viscosity of $24 \cdot 10^{-3} \text{ Pa s}$.

The problem with using these cylindrical particles is that the asymmetric cylinders with jagged edges do not have the same symmetries as the triaxial particles. Triaxial particles with distinct a_2 and a_3 have 2-fold rotational symmetry around the minor, semi-major and major axis. Cylinders with jagged edges have no such rotational symmetry. We do not know how this symmetry difference effects the equations of motion and in consequence the orbits, Poincaré maps, and winding numbers. We assume that we can approximate a jagged cylinder with a triaxial particle: Further theoretical development will prove if this is correct or not.

A problem in finding and tracking a particle was that the surface of the PDMS was very uneven

3.3. AUTOMATED TRACKING

and sharp ridges along the length of the channel appeared as seen in Figure 3.8a unless the focus was in a narrow depth of the channel.



(a) An unusually severe case of the PDMS ridges creating noise.

(b) After being polished there is no trace of ridges in the PDMS.

Figure 3.8: The effects of polishing the channel using emery cloth and a silicate abrasive. (a) Shows sharp lines along the length of the channel disturbing tracking, (b) no ridges can be seen.

To solve this the copper mold in which the PDMS channels are formed was polished with a silicate abrasive (Autosol) and emery cloth. This removed all visible scratches from the mold and therefore from the PDMS, as seen in Figure 3.8b.

3.3 Automated tracking

Most of the time making measurements was spent manually tracking a particle using the movable stage as described in section 3.1. Depending on the flow rate and the number of stretches desired for a particle, it could take up to several hours to compile one measurement. One important way to improve the setup from the previous iteration is as discussed by Johansson [3], to automate the camera tracking. This speeds up measurements and allow for a larger data set to be gathered.

A tracking algorithm was implemented using Python and the external packages **OPENCV**, **NumPy**, **SciPy**, **ImageMagick** and **ctypes**. The goal of the tracking was relatively similar to the tracking described in 4.1 and more in detail in Johansson [3]. The main difference between the tracking in this section and the one in Johansson is that the tracking described in this section moves the

actual stage, and control the pump in real time. Johansson's tracking tracks the particle in the movie after manual measurements have been made. These differences produces different problems and solutions which are detailed below.

3.3.1 Acquiring the image

The first step in tracking a particle is to acquire the image from the microscope in order to identify (and track) the particle. However the Leica DFC350 FX camera only works with the proprietary Leica software which has no API. This means that there is no way to get the image straight from the camera in real time. To solve this the `ImageGrabber` package in `Python` is used to take screenshots as often as possible. The camera image is isolated from the full screenshot by cropping the image from the proprietary software from the screenshot. This in itself is a very short program however it still takes ca 50ms per frame on an Intel Core i5 processor. Each frame is stored as a matrix \mathbf{F} with brightness values ranging from 0 to 255.

3.3.2 Reducing noise

In order to reduce noise from the image we first reduce the static noise caused by dirt, scratches and other defects in the microscope and on the camera lens, as shown in Figure 4.1a. As the noise is static it is the only thing that remains if we compute an average image $\bar{\mathbf{F}}$. After taking N images and denote them $\{\mathbf{F}_1, \mathbf{F}_2, \dots, \mathbf{F}_N\}$ the average image $\bar{\mathbf{F}}$ is given by

$$\bar{\mathbf{F}} = \frac{1}{N} \sum_{i=1}^N \mathbf{F}_i. \quad (3.2)$$

An example of such an average image can be seen in Figure 4.1b. The static noise is then removed from each frame using eq (3.1) from Johansson [3].

$$\widetilde{\mathbf{F}}_i = \mathbf{F}_i - \bar{\mathbf{F}} + (F_i^* \mathbf{I}) \quad (3.3)$$

where F_i^* is the average brightness of the frame \mathbf{F}_i , $\widetilde{\mathbf{F}}_i$ is the corrected frame and \mathbf{I} is a matrix of ones. The result can be seen in Figure 4.1c.

3.3.3 Contour detection and selection

The edges of the captured image are detected using the Canny edge detector from the OpenCV package. The canny edge detector uses two different threshold values for finding edges, τ_1 and τ_2 with $\tau_1 > \tau_2$. The larger threshold τ_1 is used for finding initial edges and τ_2 is used on pixels adjacent to ones already found. For more details on how the Canny Edge detector works see the original paper by Canny from 1986[28].

Once an edge image has been generated, we use the OpenCV command, `Contours` which returns a list of every contiguous group of edge pixels. We denote these contours $\{\mathbf{C}_1, \mathbf{C}_2 \dots \mathbf{C}_M\}$ and each contour contains M_c^i pixels, $\mathbf{C}_i = \{\mathbf{p}_1^i, \mathbf{p}_2^i \dots \mathbf{p}_{M_c^i}^i\}$. If the image is not too noisy and we have chosen the threshold values to the edge detection correctly, this includes the particle as one of the contour.

In order to identify the particle contour a few techniques are used. First, contours whose total size M_c^i is less than some minimum value, n_{min} or larger than some maximum value n_{max} are ignored. Then the average position \mathbf{P}_i of each contour C_i is calculated as the average pixel position

$$\mathbf{P}_i = \sum_{j=1}^n \mathbf{p}_j / n$$

which is used to find the distance D_i between each position \mathbf{P}_i and the expected position \mathbf{E} . The expected position is the center of the image in the first frame and thereafter we assumed the particle has the same velocity as it did the last frame. So we have

$$D_i = \|\mathbf{P}_i - \mathbf{E}\|$$

Next, a 'thinness value' for each contour ζ_i is calculated using

$$\zeta_i = \left(\frac{d_{i,max}^2}{M_c^i} \right)^2, \quad (3.4)$$

where $d_i^{(max)}$ is the longest distance between two pixels in the contour C_i .

3.3. AUTOMATED TRACKING

Finally a weighted score S_i is assigned to each contour based on its position and thinness using

$$S_i = w_{thin}\zeta_i + \frac{w_{pos}}{D_i} \quad (3.5)$$

where w_{thin} is a weighting constant for the thinness and w_{pos} is a weighting constant for the position. The contour with the highest score is chosen unless it is lower than some worst acceptable score S_{min} .

3.3.4 Adjusting the camera velocity

After the particle has been detected two times at positions $\mathbf{P}(t_0)$ and $\mathbf{P}(t_1)$, the change in position is the relative velocity $\mathbf{v}_{rel} = \mathbf{P}(t_1) - \mathbf{P}(t_0)$. The velocity of the step engine as \mathbf{v}_{step} and the correctional change in velocity of the step engine \mathbf{v}_{corr} .

If the velocity is larger than some threshold v_{thresh} the step engine velocity is changed by

$$\mathbf{v}_{corr} = \zeta \mathbf{v}_{rel}$$

where $\zeta < 1$ is damping to prevent too sudden changes. If the position of the particle is too far from the center of the image the velocity of the step engine is changed by .

$$\mathbf{v}_{corr} = \frac{\mathbf{P}(t_1)}{|\mathbf{P}(t_1)|} v_\epsilon$$

where v_ϵ is a small incremental velocity.

3.3.5 Time considerations

A higher frame rate allows for greater predictive power and increased stability as the error between frames is reduced. Reducing computational time of each task is important for optimizing the tracking, which also means knowing what tasks are the most demanding. A list of the different tasks and their average execution times can be seen in table 3.1

3.4. SUMMARY OF IMPROVEMENTS

Task	Average time (ms)	Std deviation (ms)
Capture screen	41	14
Find edges	78	23
Change velocity	230	62

Table 3.1: The average time taken for the major components of the tracking in ms. The largest fraction of time is spent in calls to the step engine using its API. This means in order to improve performance noticeably in order to double the framerate, a new way of communicating with the step engine must be devised.

We see that the FPS is limited primarily by three routines: The screen capture routine, the change velocity routine and finally the save position routine. The first and last are unavoidable and must be done every frame by definition if we are interested in knowing the particles position as well as possible. This means we simply want to use the velocity correction as little as possible. Since the time constraint is in the communication with the step engine, there is not any optimization to be done here, at least not within the scope of this thesis.

3.4 Summary of improvements

To conclude we return to the problems listed in section 3.2

1. The particles are now all symmetric to be used for measurements
2. The particles have low aspect ratios and uniform widths allowing which makes accurate estimations of size possible
3. The lower aspect ratios means there are more flips that can be used to estimate the orbit.
4. Particles are made from glass meaning they can be trapped using optical tweezers.
5. The PDMS in the channel is now smooth enough to not be noticed with the microscope.
6. Manual tracking is still necessary when tracking with the optical tweezers.

3.4. SUMMARY OF IMPROVEMENTS

7. Bubbles are still an issue, but occur less frequently as one gets more experienced in setting up the experiment.

Part II

Data analysis and results

4

Data analysis

Once a measurement has been made and a movie recorded the orientational dynamics are estimated. The first step is to identify the particle and approximate its position and orientation at every point. This is done using software from Johansson [3] and is explained in detail in his thesis and summarized below.

4.1 Particle identification

The first step of the data analysis is to reduce the static noise from the movie caused by dirt, scratches and other defects in the microscope and on the camera lens as can be seen in Figure 4.1a. As the noise is static and the actual contents of the image changes the noise is isolated by computing an average frame of all frames in a movie using equation 3.2

An example of such an average frame can be seen in Figure 4.1b. The average frame is removed from the camera frame and the result can be seen in Figure 4.1c. After this we apply a gaussian smoothing function and Canny edge detection [28] and fill the resulting edge located closest to the previous particle location. The resulting pixels are then fit to an ellipse as described in [3, 29], the ellipse is defined by a length l_e , width D and an angle ϕ_p from the x -axis. Note that ϕ_p is The filled

contour and the fit ellipse can be seen in Figure 4.1d.

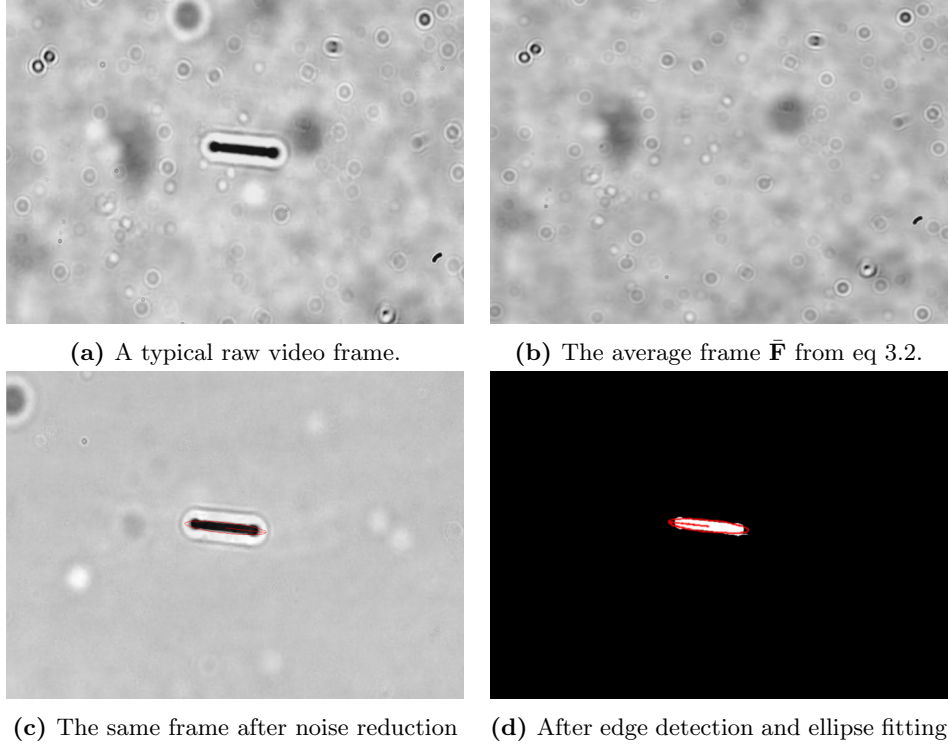


Figure 4.1: These pictures illustrate the most important step of the image analysis from raw image to estimated particle position. First the static noise from the average frame $\bar{\mathbf{F}}$

4.2 Estimation of orientation

The ellipsoid given by the fitting is then our best approximation of the projection in the x - z plane.

The projection of the particle along the x -axis and z -axis are found by

$$p_x = l_e \sin(\phi_p) \quad (4.1)$$

$$p_z = l_e \cos(\phi_p) \quad (4.2)$$

Here p_x and p_z are the x -axis and z -axis projection respectively.

To find the unit vector \mathbf{n} we need to know the length of the particle. It was shown by Leal [10]

that the particle always spends a majority of its time aligned with the flow, ie aligned with the camera plane. This means that by finding the ellipse length l_e every frame and finding the mode of the distribution we find a good estimate of L . We find the orientation vector \mathbf{n} from Section 2.3 by normalizing the projections

$$n_x = \frac{p_x}{L}, \quad (4.3a)$$

$$n_z = \frac{p_z}{L}, \quad (4.3b)$$

$$n_y = \sqrt{1 - n_x^2 - n_z^2}. \quad (4.3c)$$

This allows us to make comparisons between theory and measurement. Until this point the data analysis is the same as that in Johansson [3].

4.3 Width compensation

We have assumed that the particle is a *thin* rod so that the projection \mathbf{p} onto the x and z -axes give us an accurate estimate of \mathbf{n} . However, when we consider that our particle is 'thick' with length l_e as well as width D , the actual unit vector we find using eq. (4.3) in the above algorithm is \mathbf{n}' . Because of the width of the particle, it appears as an ellipse even when $n_z = n_x = 0$ as shown in the lower right part of Figure 4.2. Looking at the points where $\phi = 0$, which are the points plotted on the surfaces of section and thus of the most interest, we find

$$\|\mathbf{n}'\| = \frac{p'_z}{L} = \frac{p_z \cos(\theta) + D \sin(\theta)}{L}. \quad (4.4)$$

Here L is the particle length and D is the particle width. The difference between the measured orientation vector \mathbf{n}' and the actual orientation vector \mathbf{n} is illustrated in Figure 4.2 for 4 different values of θ .

In order to compensate for the width of the particle we modify our projection equation 4.1 to

$$p_x = (l_e - D) \sin(\phi_p) \quad (4.5)$$

$$p_z = (l_e - D) \cos(\phi_p) \quad (4.6)$$

Using eq. (4.5) reduces the particles estimated length by D but this is solved by normalizing with $L - D$ instead of L in 4.3.

This change completely removes the error for $n_z = 0$ which is when the error is largest. It does however cause slight distortions in the orbit and a better method could be devised.

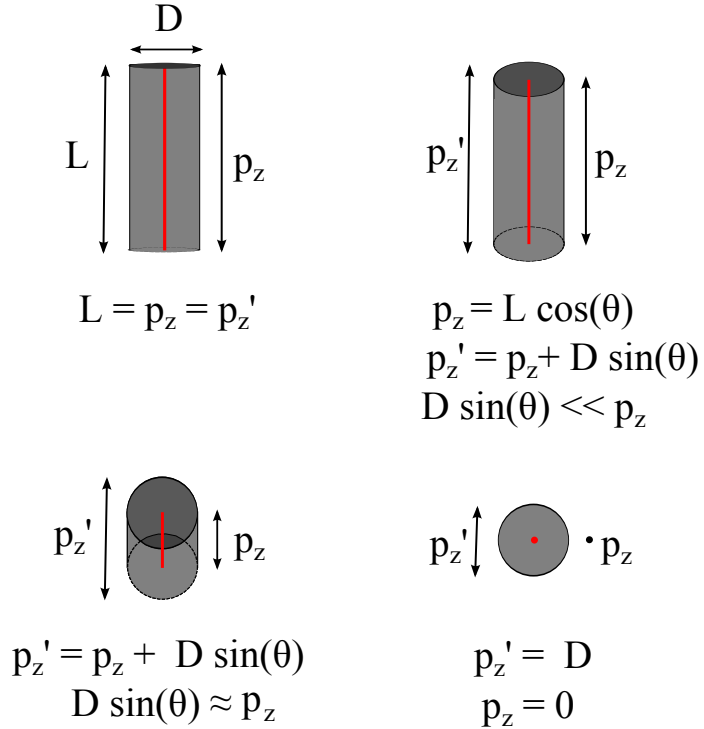


Figure 4.2: Shows the incorrect projection vector \mathbf{p}' we obtain from incorrectly assuming the particle is 'thin' in eq. 4.1. The correct projection vector is highlighted in red. Shows four different θ angles at $\phi = 0$.

4.4 Removing tracking errors

The tracking typically contains a few frames where the particle is not detected correctly due to being visually obstructed in some way. This causes spikes in the data which complicates analysis. To make further theoretical analysis possible the data is corrected by removing such points manually. The basis for removal is a large discontinuity in the data, and many such points could be eliminated with algorithmic means. However in particular for n_z it is very difficult to write an algorithm that catches all possible edge cases without having false positives. For example n_z have peaks that make its derivative non continuous which means that a continuous derivative cannot be used to exclude points. It's was found to be simpler to look at the analysis program and remove the points where the particle cannot be traced accurately due to noise.

An example of data before and after correction can be seen in Figure 4.3 and all uncorrected data files of measurements used in this thesis are available at <http://goo.gl/jgzSXe>.

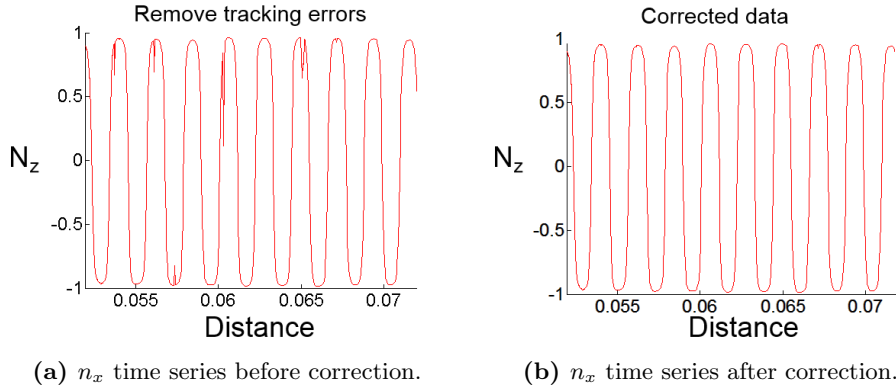


Figure 4.3: Shows screenshots from the software used to remove tracking errors for a time series of n_z before and after removing points where a significant amount of noise disturbed the tracking.

4.5 Estimating the winding numbers

As discussed in section 2.3.1, estimating the winding number for different types of orientational orbit for one particle allows for a better estimation of ϵ . In order to estimate the winding number for a measured particle we must identify the two periods θ_1 and θ_2 from Figure 2.7.

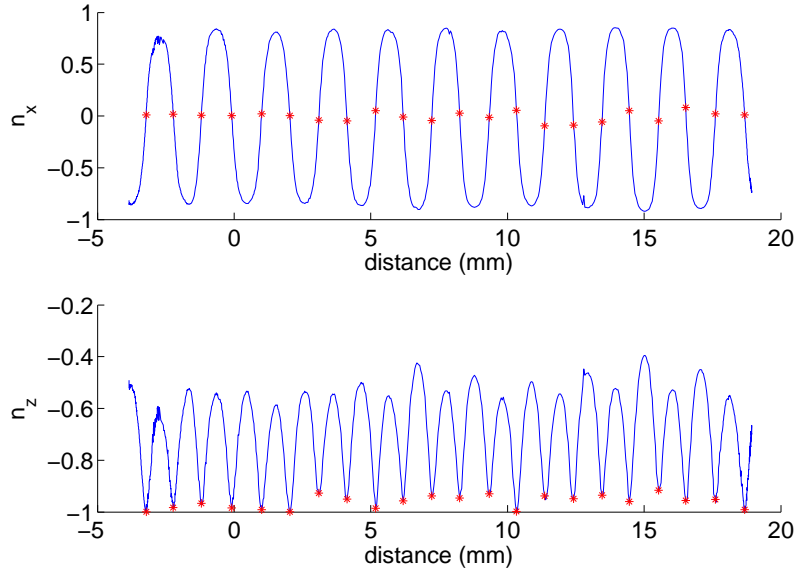


Figure 4.4: The stars are plotted at the same distances in the n_x and n_z plots. We see that zeros of n_x and maxima of n_z occur almost exactly at the same points. These points are referred to as \mathbf{P}_z

The maxima with the shorter period θ_2 are located where $n_x = 0$ as is seen in Figure 4.4. We denote the set of these points P_z . The longer period θ_1 is the periodicity of P_z , marked as red points in Figure 4.4. To estimate the winding number we want to locate the maxima M and minima m in P_z that occur with period θ_1 in the same way we do to find θ_2 in n_z . Unfortunately the height of peaks are noisy and there are few data points for each measurement as the channel is of finite length only allowing a few dozen flips. This means averaging cannot be used to reduce the noise. This means we have no algorithmic means to find θ_1 .

Instead we select a number of maxima M_1, M_2, \dots, M_p and minima m_1, m_2, \dots, m_q from \mathbf{P}_z . We denote their index in n_z as $I_1^M, I_2^M, \dots, I_p^M$ for the maxima and $I_1^m, I_2^m, \dots, I_q^m$ for the minima. We then find θ_1 as the mean distance between successive maxima $\overline{d_M}$ and successive minima $\overline{d_m}$,

$$\overline{d_M} = \frac{1}{p-1} \sum_{j=1}^p I_{j+1}^M - I_j^M \quad (4.7)$$

$$\overline{d_m} = \frac{1}{q-1} \sum_{j=1}^q I_{j+1}^m - I_j^m \quad (4.8)$$

$$\hat{\theta}_1 = \frac{\overline{d_M} + \overline{d_m}}{2}. \quad (4.9)$$

In the case that we only have 1 maxima and minima eq. 4.9 can't be calculated so we assume that the distance between a maxima and minima is half a period, i.e.

$$\hat{\theta}_1 = 2 |I_1^M - I_1^m| \quad (4.10)$$

4.6 Matching data to theoretical orbits

To verify that the theoretical orbits from Section 2.3 have been measured we want to match the measurements to theoretical orbits.

To find the best matching orbit from a Poincaré map for a measurement we again utilize \mathbf{P}_z , the points where n_z peaks and $n_x = 0$. We denote the length of \mathbf{P}_z as N . We are concerned with matching them with the peaks from theoretical orbits.

To find the best matching theoretical orbit for a measurement we compute the least square distance between \mathbf{P}_z and all orbits on all phase maps with ϵ in the range $[0.01, 0.02, \dots, 0.1]$ for 200 consecutive initial ψ (the x -axis on the Poincaré map). If we for each orbit denote the theoretical series of n_z peaks as $\mathbf{Q}_z(\theta, \epsilon)$. We make sure that the length of $\mathbf{Q}_z(\theta, \epsilon)$ be twice that of \mathbf{P}_z which guarantees that we always find the correct phase. We define $\mathbf{Q}_z(\theta, \epsilon, i)$ to be the n_z series $\mathbf{Q}_z(\theta, \epsilon)$ starting at index i . We assign a score function $S(\theta, \epsilon, i)$ as

$$S(\mathbf{P}_z, \theta, \epsilon, i) = \frac{1}{N} \left| \mathbf{P}_z - \mathbf{Q}_z^{(i)}(\theta, \epsilon) \right|^2. \quad (4.11)$$

An example experimental P_z series matched to theoretical data is seen in Figure 4.5.

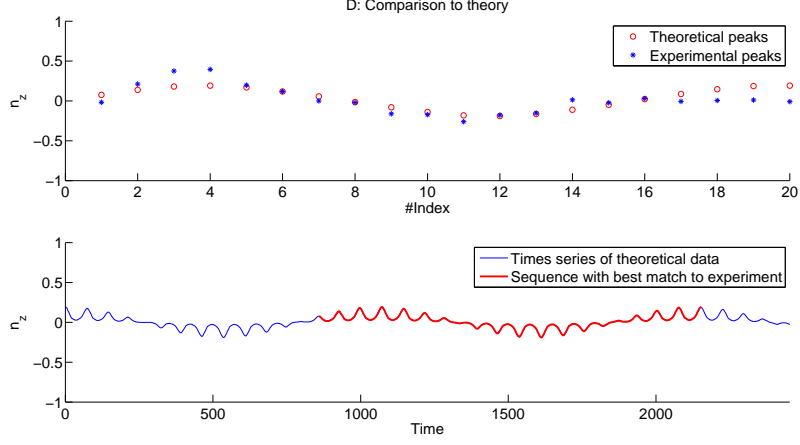


Figure 4.5: The upper figure shows the experimental n_z peaks \mathbf{P}_z and the theoretical peaks \mathbf{Q}_z for the best matching orbit. The lower plot shows where what section of the theoretical time series was used for matching, ie what i from section 4.6 was chosen.

Over r different measurements $\mathbf{P}_z^{(1)}, \mathbf{P}_z^{(2)}, \dots, \mathbf{P}_z^{(r)}$ we expect the initial conditions θ and i (the phase) to change. The asymmetry ϵ does not change between measurements. So for each ϵ we find the best θ and i using the temporary score function $\hat{S}(\mathbf{P}_z^{(j)}, \epsilon)$

$$\hat{S}(\mathbf{P}_z^{(j)}, \epsilon) = \min(S(\mathbf{P}_z^{(j)}, \theta, \epsilon, i)) \quad (4.12)$$

and then find the best ϵ for a particle using

$$\epsilon_{best} = \min \left(\sum_{j=1}^r \frac{\hat{S}(\mathbf{P}_z^{(j)}, \epsilon)^2}{N^{(j)}} \right). \quad (4.13)$$

It is important to note that this matching has a theoretical limitation. The asymmetry of our cylindrical particles is different from the asymmetry in the triaxial particles used in the theoretical models. The triaxial particles still have a rotational symmetry for rotations of π around any of the major/minor axes. This is not the case with the asymmetric cylindrical particles, which have no

rotational symmetry. We therefore have to make the assumption that the difference between these two types of asymmetry is not significant and further theoretical work might reject this assumption.

5

Results

The aim of these measurements is to show that the particles follow Jeffery orbits and to show that they exhibit quasi-periodic and periodic motion for different initial conditions. In order to show that there are no significant disturbances we examine the dynamics of the particles during reversal of the flow. If the particle reverts its dynamics perfectly there have been no noise or inertial effects affecting the rotational motion.

During the work of this thesis a large number of movies of particles have been recorded with gradual improvements to the setup primarily in terms of density matching, particle density (the number of particles per liquid volume) and bubble elimination.

In this section we present the data from two different particles. These were the only particles where there were reversals that retraced their movements closely for several stretches for both quasi-periodic and periodic orbits. One is referred to as particle A, the other as particle B. Particle A is approximately $24 \mu m$ long so it has an aspect ratio $\lambda \approx 8$. Particle B is approximately $20.5 \mu m$ long so it has an aspect ratio $\lambda \approx 7$. The measurements in this section were done together with Alexander Laas [2].

We started each measurement at an approximate depth D and at position $p_0 = (x_0, z_0)$ in the channel relative to the inlet on the right, closer to the pump.

5.1 Measurements

5.1.1 Measurements of particle A

Particle A was measured on October 11 in 2013. Two of the measurements retraced their orbits closely before and after reversals: measurement 1 and measurement 2 which can be seen in Figure 5.1 and Figure 5.2 respectively. Measurement 1 was started with initial condition $n_z \approx 0$ and showed quasi-periodic behaviour with a periodic change in amplitude for n_z peaks. Measurement 2 was started with initial condition $n_z \approx 1$ and showed periodic behaviour with very constant n_z peaks.

Other measurement had reversals where the orbit changed considerably, two examples are seen in Figure 5.3 and 5.4. All measurement data for particle A can be found at goo.gl/jgzSXe where particle A is referred to as particle 2 from October 11.

Measurement 1

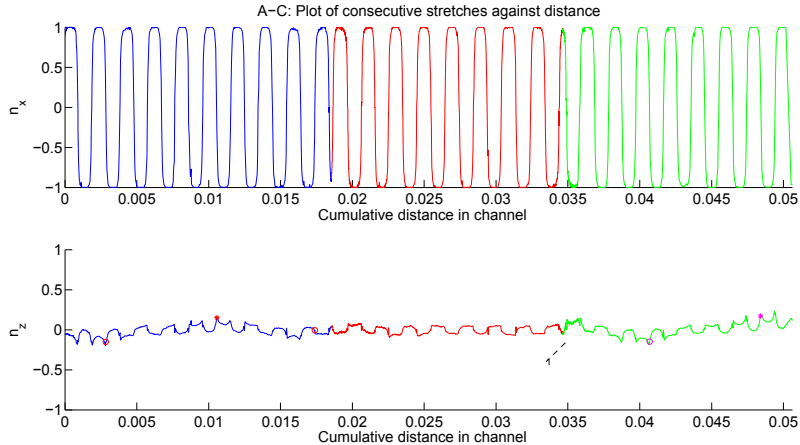


Figure 5.1: The n_x and n_z components of the particle for measurement 1 against cumulative distance in channel. Despite being very close to a centre orbit there is limited quasi-periodic behaviour as the peaks stay close to 0. The very flattened peaks compared to a low n_z orbit in 2.4b are a result of the width compensation discussed in section 4.3. The circles and stars indicate n_z peaks used for estimating the winding number. This particle started $x_0 = 9.8\text{mm}$, $z_0 = 8.9924\mu\text{m}$ and $D \approx 90\mu\text{m}$. This is the same measurement as is used in Figure 6.20 in Laas thesis [2]

5.1. MEASUREMENTS

Measurement 2

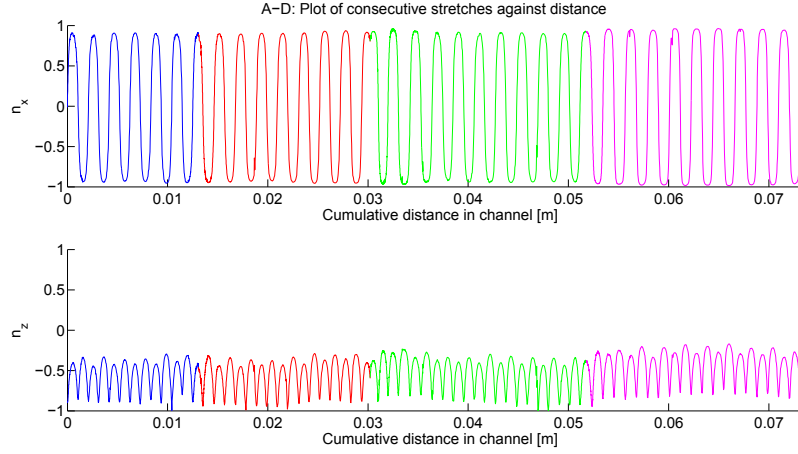


Figure 5.2: The n_z and n_x components for measurement 2 against cumulative distance. The n_z component is consistently close to 1 at the peaks. The particle started at $x_0 = 26.0\text{mm}$, $z_0 = 275\mu\text{m}$, $D \approx 105\mu\text{m}$. This figure is the same as Laas [2] Figure 6.21

Measurement 3

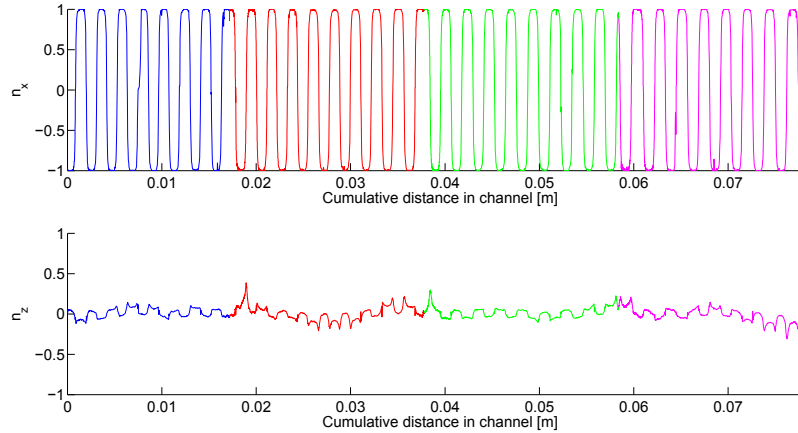


Figure 5.3: The n_z and n_x components for measurement 3 against cumulative distance. The larger peaks that occur after the reversals are not caused by a tracking error but can be seen clearly in the films. The reversal of the flow is started when the particle is next to the point marked (3) which is also where there is an unexpected change in n_z component. The particle started at $x_0 = 12.3\text{mm}$, $z_0 = 160\mu\text{m}$, $D \approx 100\mu\text{m}$.

Measurement 4

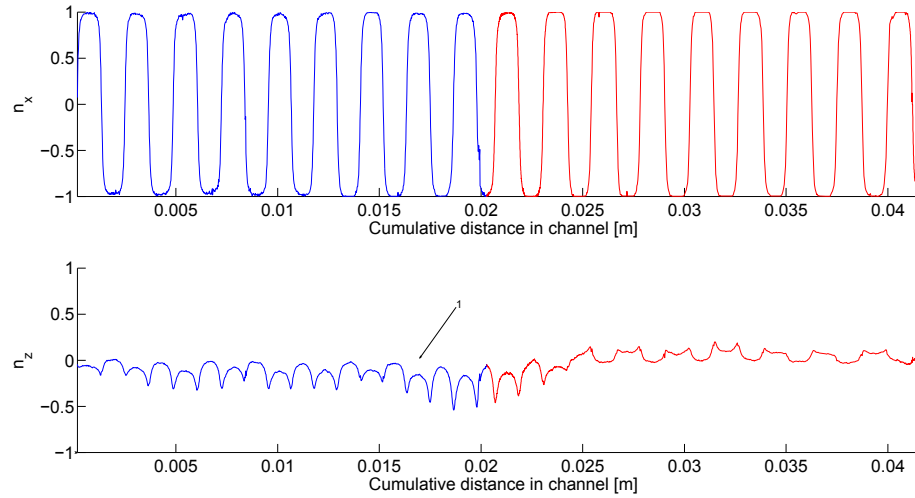


Figure 5.4: The n_z and n_x components for measurement 4 against cumulative distance. The flow is reversed when the particle is at the point marked by (1) and we can see that the peaks around the reversal are larger than for the rest of the measurement. Started at $x_0 = 8.7\text{mm}$, $z_0 = 16\mu\text{m}$, $D \approx 95\mu\text{m}$.

Measurement 5

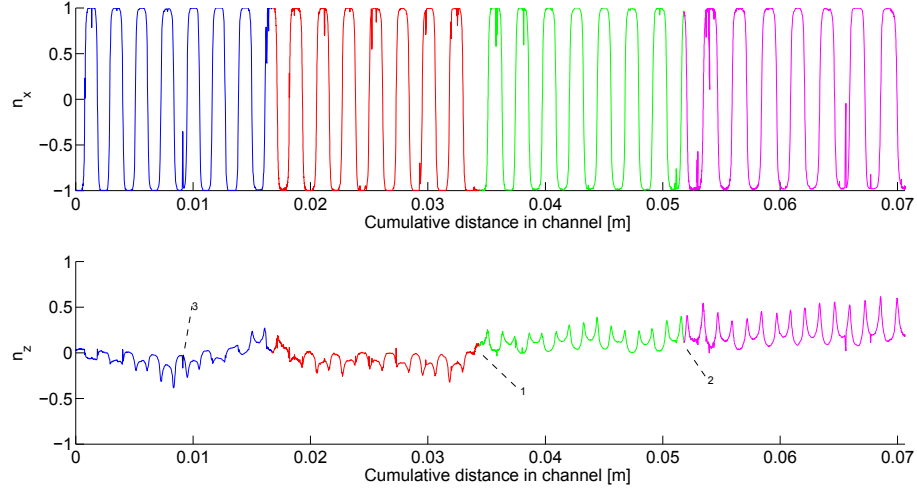


Figure 5.5: The n_z and n_x components for measurement 5 against cumulative distance. At the point marked by (1) n_z changes drastically at the reversal which occurs at the side of the channel closer to the pump. Although there is also some change in the orbit at the reversal marked by (2) it does not move comparably far on the S.O.S. There are a number of small peaks in the data such as the one indicated by (3) which is a consequence of insufficient removal of tracking errors, see Section 4.4. The particle started at $x_0 = 10.7\text{mm}$, $z_0 = 240\mu\text{m}$, $D \approx 60\mu\text{m}$.

5.1.2 Measurements of particle B

Particle B was measured on October 1 2013. Particle B has four measurements for which most reversals showed little change in orbit. These are shown below in Figures 5.6, 5.7, 5.8 and 5.9. There were also problematic measurements of particle B analogous to those for particle A, but they have not been included in this section for brevity. All measurement data for particle B can be found at goo.gl/jgzSXe where particle B is referred to as particle 4 from October 1.

Measurement 1

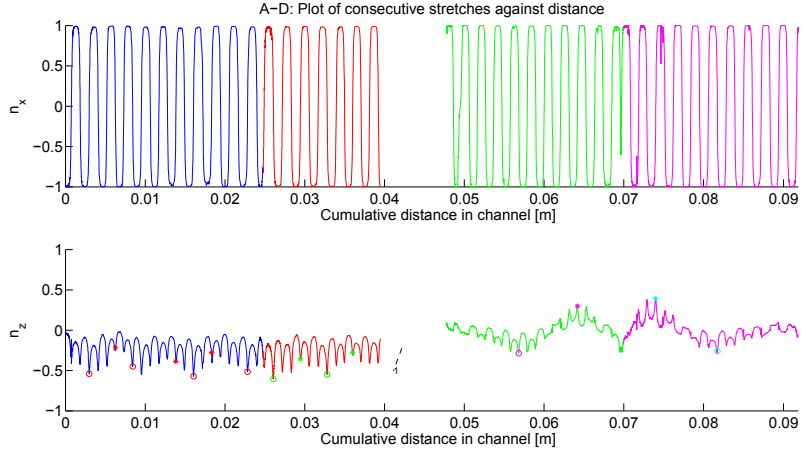


Figure 5.6: The n_z and n_x components for measurement 1 against cumulative distance. The first two and the last two stretches the particle retraces its motion very closely during the reversals. In the reversal between these two reversals there is a large change in orbit which begins at (1) where the flow is starting to revert. This reversal occurs at the end of the channel closer to the pump. The circles and stars indicate n_z peaks used for estimating the winding number. Starts at $x_0 = 9.3\text{mm}$, $z_0 = 35\mu\text{m}$, $D \approx 100\mu\text{m}$. This is the same measurement as is used in Figures 6.2 and 6.4 in Laas thesis [2]

Measurement 2

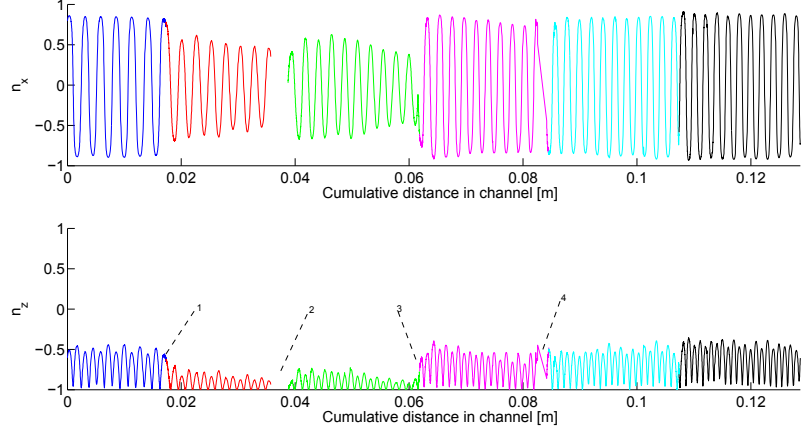


Figure 5.7: The n_z and n_x components for measurement 2 against cumulative distance. The orbit is mostly constant orbit with $n_z \approx 1$ at the peaks. The reversals at (1) and (3) both change the orbit slightly however the difference between the peaks is small and the best matched theoretical orbits in Figure 5.17 are similar before and after reversals. There is missing data at (2) and (4) where the particle was no able to be tracked. The particle started at $x_0 = 28.6\text{mm}$, $z_0 = 72\mu\text{m}$, $D = \approx 85\mu\text{m}$. This is the same measurement as is used in Figure 6.8 in Laas thesis [2]

Measurement 3

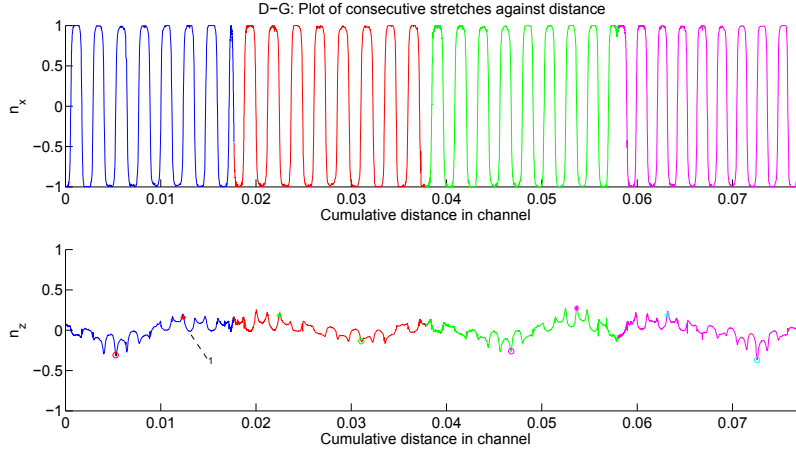


Figure 5.8: The n_z and n_x components for measurement 3 against cumulative distance. The initial condition is $n_z \approx 0$ and the sign changes periodically. The circles and stars indicate n_z peaks used for estimating the winding number. Started at $x_0 = 2.7\text{mm}$, $z_0 = 76\mu\text{m}$, $D \approx 90\mu\text{m}$. This is the same measurement as is used in Figures 6.10 and 6.12 in Laas thesis [2]

Measurement 4

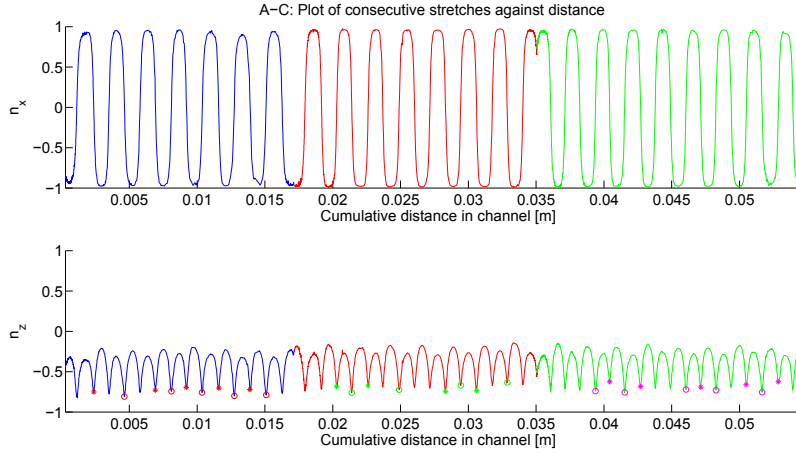


Figure 5.9: The n_z and n_x components for measurement 4 against cumulative distance. The changes in n_z are not large, but there is a periodic variations that could correspond to a sign preserving quasi-periodic orbit. The circles and stars indicate n_z peaks used for estimating the winding number. Started at $x_0 = 12.9\text{mm}$, $z_0 = 21\mu\text{m}$, $D \approx 85\mu\text{m}$

5.2 Diagnostic plots

A number of diagnostic measurements were made for each particle to find possible problems with the setup. In this section we only show the diagnostic measurements from measurement 1 for particle A, and from measurement 2 for particle B but all diagnostic plots can be found at <http://goo.gl/jgzSXe>.

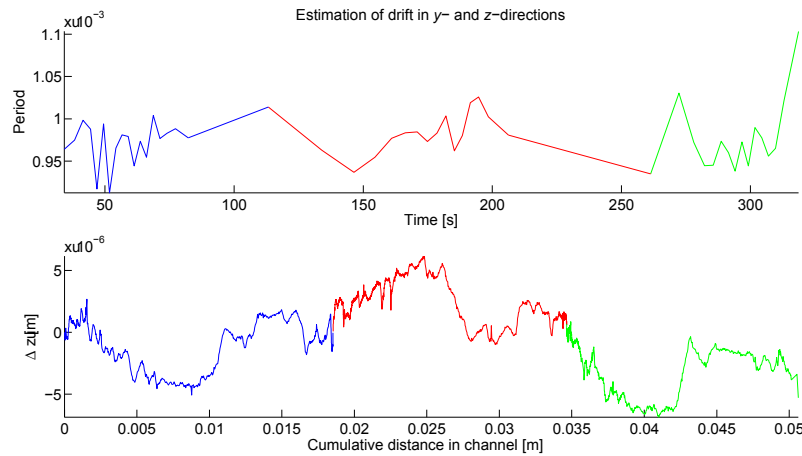


Figure 5.10: The estimation of drift in y and z direction for Particle A from measurement 1. Upper figure is the estimation of the sinking of the particle, the lower figure is the measured z position in the channel against cumulative distance.

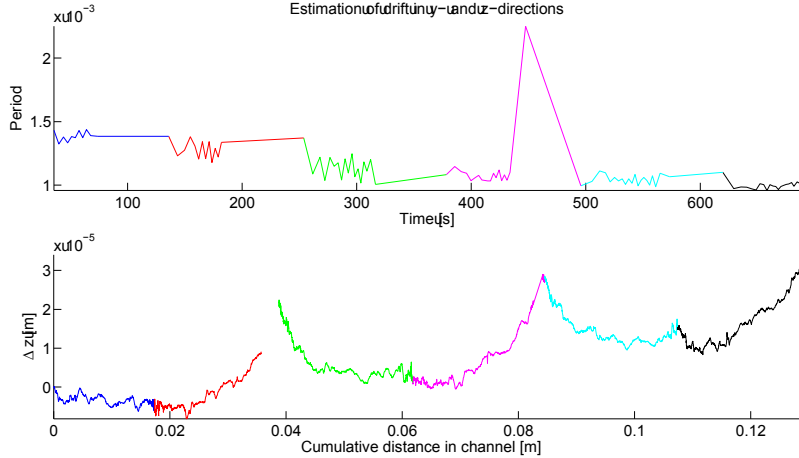


Figure 5.11: The estimation of drift in y and z direction for Particle B from measurement 2. Upper figure is the estimation of the sinking of the particle, the lower figure is the measured z position in the channel against cumulative distance. The large peak that occurs between 400 and 500 seconds is caused by not being able to track the particle during this time which causes the estimated period to be approximately twice as high as it is.

The centre of mass movement in the direction perpendicular to the flow direction x is seen in Figures 5.10 and 5.11. Movement in the y direction, i.e. sinking or floating, was measured by plotting the period of each flip against time as in the upper figure. The period here refers to the distance Δ_i between two successive zeros for n_x relative to the first such distance Δ_0 . If there is no clear trend to higher or lower values it implies that there is little sinking or floating.

The movement in the z coordinate is very small relative to the movements in the x direction. We can see that Z -direction movements along one stretch are on the order of $10\mu\text{m}$ compared to the x direction which is on the order of $2 \cdot 10^4\mu\text{m}$. The change in period was less than 20% for all particles presented in this chapter.

The speed was plotted as a function of time to see how the flow reversed and if there were any problems with the pump. There is a noticeable difference between reversals that occur on the side of the channel and the side closer to the pump where on the reversal on the end of the channel further from the pump the speed drops to 0, increases for a short while and then goes back down to 0. This has been a consistent feature across all measurements.

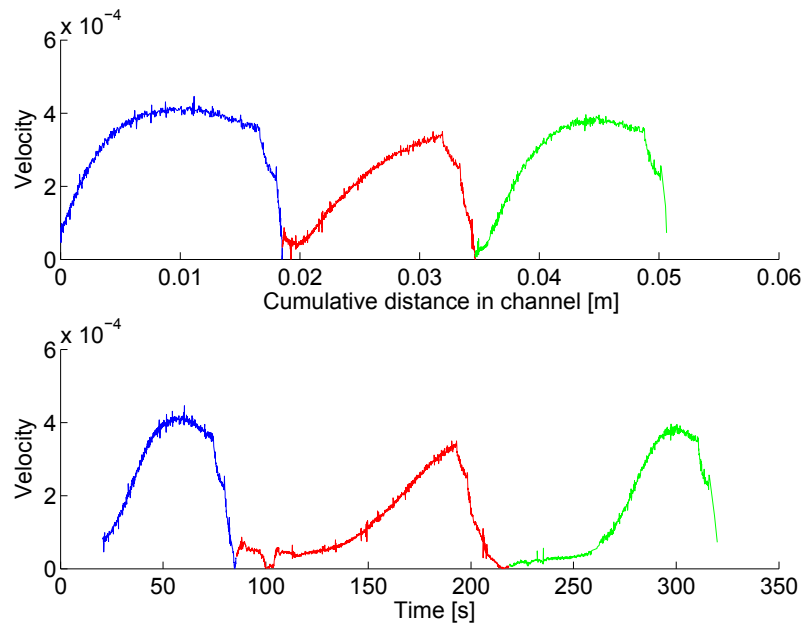


Figure 5.12: The speed (note not the velocity) of the particle A from measurement 1 against cumulative distance in the upper figure and against time in the lower figure.

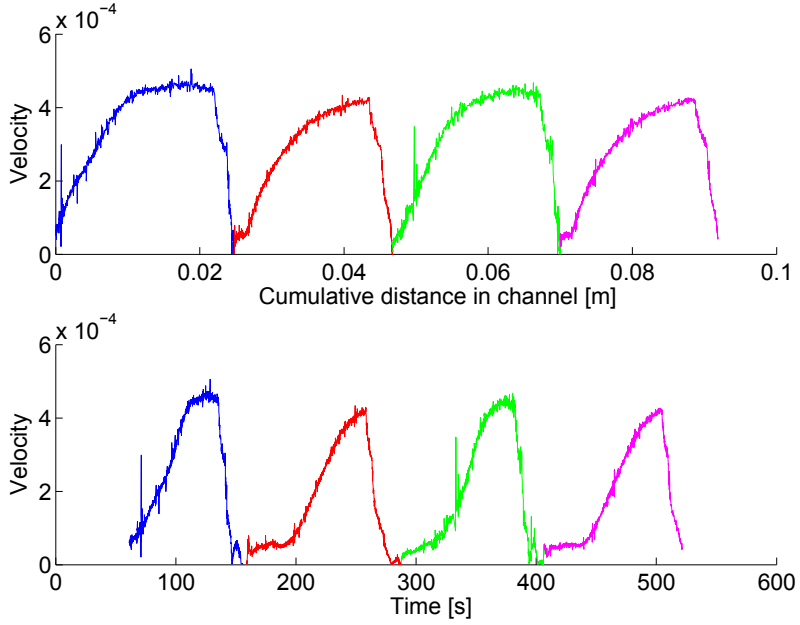


Figure 5.13: The speed (note not the velocity) of particle B from measurement 2 against distance in the upper figure and against time in the lower figure. In the plot against time there is an extra dip to 0 at around $t = 150$ and $t = 400$. This occurs at the end of channel further away from the pump.

5.2.1 Reversals

In order to show that the dynamics of the particle revert when the flow is reversed we plot the components of \mathbf{n} against distance in the channel. The first reversal from measurement 1 for particle A is seen in Figure 5.14. The n_z components are very similar along the entire length of the channel only at the very end does there is there a difference larger than the margin of error. The same plot is made from the second reversal from measurement 5 in Figure 5.15. Here the particle changes orbit drastically at the reversal while being stable before and after.

5.2. DIAGNOSTIC PLOTS

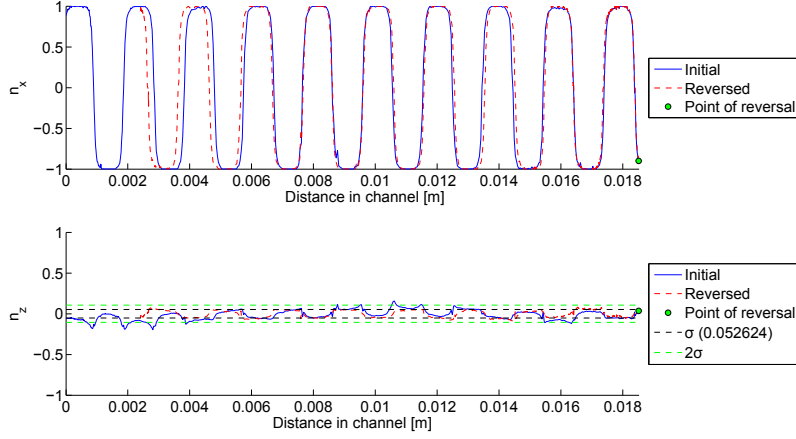


Figure 5.14: Shows n_x and n_z first and second stretches from Measurement 1, seen in Figure 5.1 but against the actual position in the channel as opposed to cumulative distance. There is an almost perfect match along the entire channel for n_x and only small disagreement for n_z . The dashed lines indicate the error margins for detecting $n_z = 0$. This figure is the same as can be seen in Laas[2] Figure 6.21

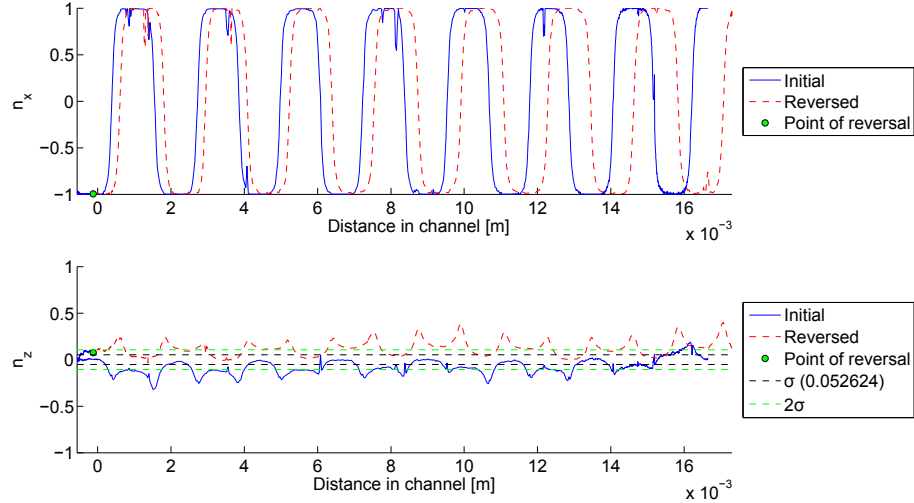


Figure 5.15: n_x and n_z from Figure 5.5 for the second and third stretch plotted against actual distance instead of commutative distance. The reversal occurs at the left and although there is some moderate agreement in n_x the match in n_z is non existant from the very start.

5.3 Match to theoretical orbits

5.3.1 Particle A

Particle A is approximately $24\mu m$ long so it has a λ close to 8 and the closest match for the asymmetry is $\epsilon = 0.02$.

Using the algorithm described in section 4.6 we match the data from measurement 1 and 2 for particle A to find the closest matching ϵ and the best matching orbits. This is shown in Figure 5.16. We can see that particle A is in a quasi-periodic sign changing orbit during measurement 1, it is matched to the lines indicating A B and C for the first, second and third stretches respectively. After being shifted by the optical tweezers, particle A followed a periodic orbit during measurement 2. Measurement 2 is matched to the orbits D, E, F and G for the first, second, third and fourth stretches respectively. The stretches that do not have winding numbers listed in the figures had orbits that did not have enough variation in n_z peaks to try to estimate a winding number.

Note that the orbits shown in Figures 5.16, 5.17, and 5.18 are not the exact orbits matched. The measurements were matched to Poincaré maps with more orbits, but due to aliasing issues of printing such Poincaré maps more sparse Poincaré map are used. Each stretch is printed on the closest matching orbit for $\psi = 0$. The winding numbers are based on the more accurate fit and the better fits are available at <http://goo.gl/jgzSXe>.

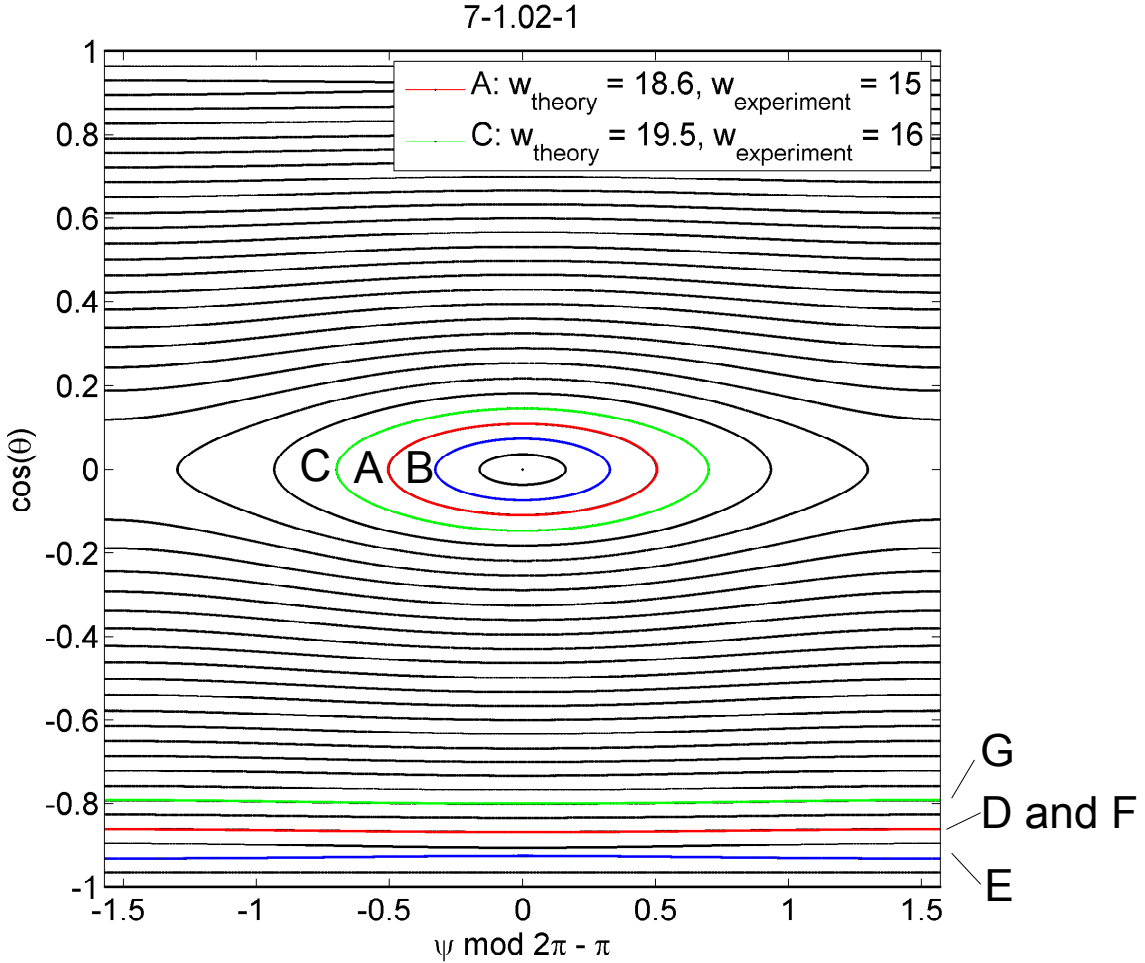


Figure 5.16: Black lines show the Poincaré map of the Jeffery's equations for $\lambda = 8$ and $\epsilon = 0.02$. The measured λ was 8.2 ± 0.1 . The orbits of the best fit theoretical fits to measurements are highlighted stretch by stretch. None of the orbits for this particle had any large variations despite being very close to $n_z = 0$. The winding numbers are within 50% of the estimates but both are too low, suggesting that the ϵ might be too low.

5.3.2 Particle B

The same procedure is repeated for particle B using the data from measurement 1,2, 3 and 4. To make the graph less cluttered it is split into two figures, Figure 5.17 for measurement 1 and 2 and Figure 5.18 for measurement 3 and 4.

5.3. MATCH TO THEORETICAL ORBITS

In Figure 5.17 particle B during measurement 1 is matched to quasi-period orbits. During stretch 1 and 2 indicated by A and B it is matched to quasi-periodic sign preserving orbits. After unexplained behaviour during a reversal stretched 3 and 4 are matched to the same sign-changing orbit indicated by C and D. After being shifted using the optical tweezers, stretches 1 through 6 during measurement 2 are matched to the highly periodic orbits indicated by E, F, G, H, I, and J respectively.

In Figure 5.18 the closest matched orbits for particle B during measurement 3 and 4 are shown. During measurement 3 the quasi-periodic sign-preserving orbits indicated by A, B and C are the closest matches to stretches 1,2 and 3. After being shifted by the optical tweezers particle B followed a sign changing quasi-periodic orbit during measurement 4. The best matching orbits for the first, second, third and fourth stretch of measurement 4 are matched to the orbits indicated by D, E, F, and G respectively.

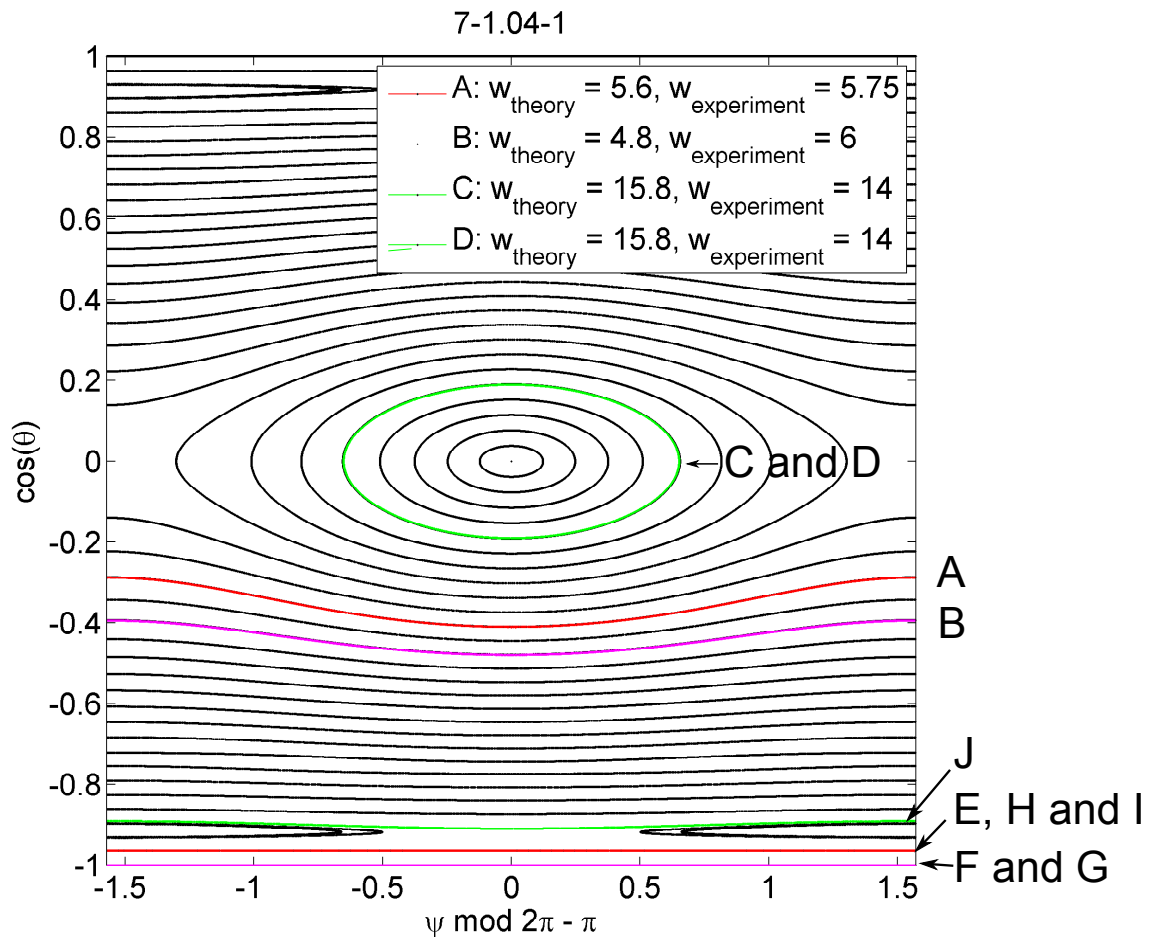


Figure 5.17: Black lines show the Poincaré map of the Jeffery's equations for $\lambda = 7$ and $\epsilon = 0.04$, the estimate of λ from measurement was 6.7 ± 0.1 . The highlighted orbits are the best fits to the stretches from measurements 1 and 2 of particle B. A-D are from measurement 1 and E-I from measurement 2.

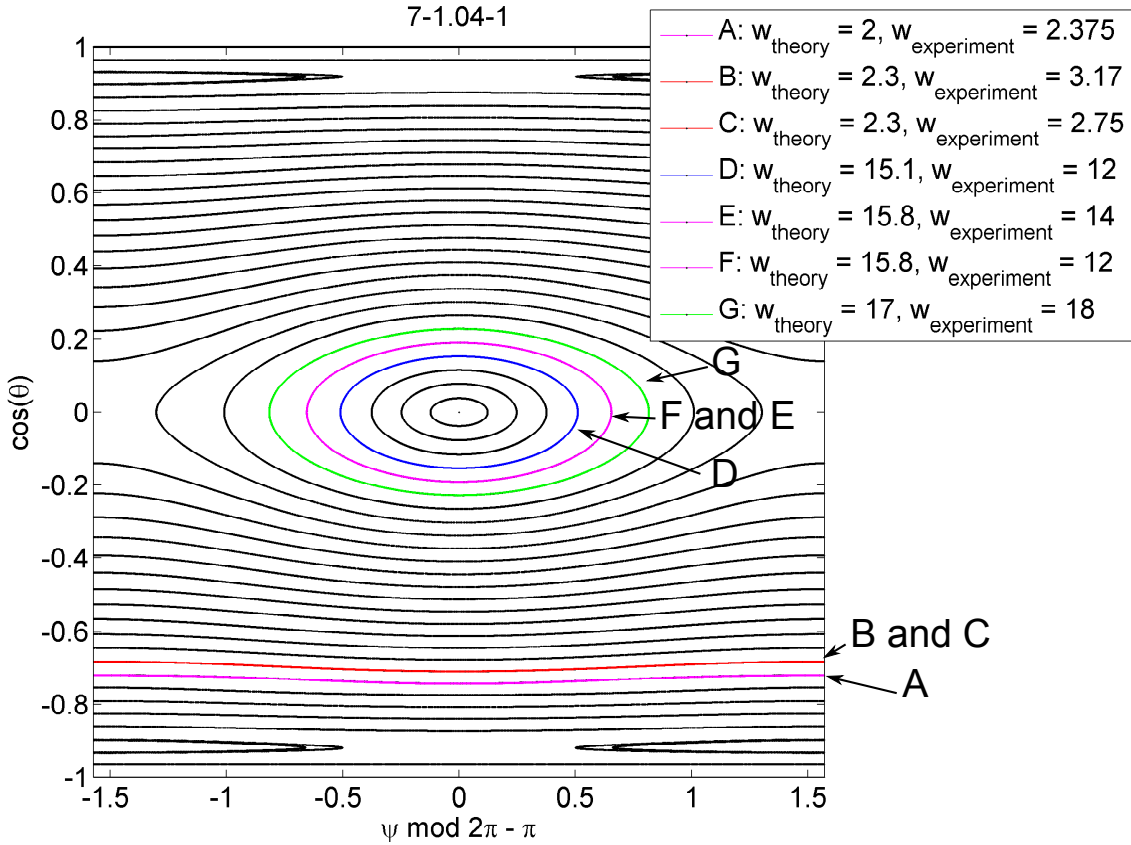


Figure 5.18: Black lines show the Poincaré map of the Jeffery's equations for $\lambda = 7$ and $\epsilon = 0.04$. The estimate of λ from measurement was 6.7 ± 0.1 . The highlighted orbits are the best fits to the stretches from measurements 3 and 4 of particle B. A-C are from measurement 3, and D-G from measurement 4.

6

Discussion

The primary goal of this thesis is to experimentally verify that asymmetric particles in shear flow exhibit different types of motion for different initial conditions, as was predicted by Yarin *et al.* [11]. To verify that there was no significant amount of noise we look at the reversal of the flow. If the particle retraces its motion it confirms a lack of noise as well as a lack of inertial effects. To estimate the asymmetry ϵ of the particles we try to match the experimental trajectories over several measurements with theoretical orbits. We also utilize the winding number of quasi-periodic orbits where it can be detected to confirm that the match is valid.

Looking at Figures 5.18, 5.17 and 5.16 we find both quasi-periodic and periodic motion as well as all three types of orbits discussed in section 2.3.1. The winding numbers for the orbits where we can measure it are within 50% of our theoretical predictions. This suggests that we have observed both quasi-periodic orbits and periodic orbits for the same particle two times. We do however have to consider the assumption we make regarding the symmetry difference between the damaged cylinders used experimentally and the flattened spheroids use in theoretical models.

Furthermore our goal was to see that different particles will exhibit different behaviour from the same initial condition based on their asymmetry. Particle A and B exhibit quite different behaviour after the same initial condition $n_z = 0$ with a noticeably lower winding number for particle B and

larger fluctuations. However with only 2 particles to compare this and only 1 good measurement for particle A it is still uncertain.

We have not been able to show a particle exhibiting chaotic motion. This might be due to the relatively small sample of good data or due to the particles being too symmetric. Based on the Poincaré maps in Johansson [3] we see that a larger region of chaotic orbits only appear when $\epsilon \geq 0.2$ and it seems possible based on Figure 3.6 and Figure 3.7 that the asymmetry is lower than this for almost all particles. But is unclear if we can make that comparison between the asymmetric cylinders and the triaxial particles used in the simulations.

These results are from a few measurements of two particles, there are many other measurements and other particles that have reversals where there are large differences before and after such as in Figure 5.15 and Figure 5.5. There are four major problems in the data

1. Sinking
2. Change in orbit after a reversal
3. Too few flips to clearly estimate winding number
4. Unexplained changes in orbit

6.1 Sinking

One of the major problems with this setup compared to the previous setup used by Einarsson *et al.* [1] is matching the density of the fluid to that of the particles. Even with a small mismatch of 0.05 g/ml we find using eq. (2.5) a sinking speed of $= 4.9 \cdot 10^3 \mu\text{m}/\text{s}$. In earlier measurements the pump speed was $3 \mu\text{l}/\text{minute}$ and the particle were 60% larger, which meant the sinking occurred during more than twice as long time because of the slower speed, and twice as fast due to the larger particles. This means it is no longer as big of a problem as during earlier measurement but it can still be noticeable in longer measurements such as in Figures 5.7 and 5.11.

6.2 Reversals where the orbit changes

Almost every measurement with several stretches have a reversal where the particle noticeably changes orbit. This can been seen in Figures 5.5, 5.4 and 5.6. While there is a trend that reversals that do not retrace their orbit occur at he end further from the pump, there are many exceptions to this. There are many cases where the orbit begins to change just as the flow is starting to reverse, such as in Figure 5.4. The particle Reynolds number depends on the velocity relative to the particle so a possible culprit could be that reversals occur too rapidly and increase the Re_p such that the $Re_p \ll 1$ condition from Jeffery [8] does not hold. We have not been able to draw any clear conclusion and solving issues with reversals would be a tremendous improvement.

6.2.1 Possible expansion of the channel

A possible cause of reversals where the people does not retrace its dynamics when the flow is reversed is that the reversals occur too quickly. A fast reversal could increase the \mathfrak{R} so that we no longer have Stokes flow. To prevent this the reversals are incremental as discussed in Section 3.1.

Making the reversals slower could solve this issue, but if we look at the speed of the particle A in Figure 5.12 and particle B in Figure 5.13 we see that after a rather sharp decline in speed when the reversal starts, the acceleration is slow. Almost all of this acceleration occurs while the pump is infusing or withdrawing at a fixed rate. The liquid in the channel accelerating while the pump rate is constant implies that there is a noticeable expansion in the channel. To verify this we look again at Figures 5.12 and 5.13.

If we have an expanded/contracted channel it has different effects on different sides of the channel. When the flow is reversed with the particle on the side closer to the pump the impact of the channel is limited as the only pressure felt by the particle is the built up pressure from the expansion/contraction of the channel. Assuming that the expansion is modest we expect this built up pressure from the channel to be significantly smaller than the one exerted by the pump. So we expect that on this side of the channel the particle reverts quickly.

However when the flow is reversed and the particle is on opposite side of the channel from the

6.3. WINDING NUMBER MATCHING

pump things are different. Most of the channel feels the pressure difference before the particle so any excess liquid in an expanded channel slows the reversal of the particle. This causes a delay where there is no acceleration for some time while after the pump reversed.

This behaviour is exactly what we see in all speed plots like 5.12 and 5.13. For reversals on the far end of the channel there is a second dip where the particle goes to $|v| = 0$, and in general reversals on the far end are noticeably slow. On the end closer to the pump this 'double dip' never occurs and accelerations are faster, but still slower than if there was no elasticity in the system.

An alternative theory for the delay in reversals is that there is an offset in the pump, a distance between the syringe handle and the pump holder which needs to be traversed before pumping actually begins. However if this was the case we would expect this delay to occur at both ends of the channel equally, and this is not what is observed. An offset in the pump does also fail to explain the long period of acceleration for the particle when the injection rate is constant.

We do not know how the slow acceleration and slow reversals impacts the dynamics of the particles, however a majority of reversals where the particle does not retrace its orbit occur at the end of the channel close to the pump. This suggests that this extra 'elasticity' in the system might in fact improve the measurements.

6.3 Winding number matching

Using the score function \hat{S} as described in section 4.6 to find the closest matching orbit gives us an estimate of the asymmetry and the orbit of the particle. But it only gives the best fit from a number of different orbits and asymmetries it does not guarantee that it is the only orbit for which there is a good match. To try and validate this we use the winding number to validate or dismiss a matched orbit and the estimated ϵ . The winding number can only be used for the orbits where n_z changes noticeably, i.e. the quasi-periodic orbits, but these are also the ones of primary interest. Figure 2.8 shows that the difference in winding number for the same θ is on the order of a factor 2 between $\epsilon = 0.01$ and $\epsilon = 0.05$ for sign-changing orbits, and still quite noticeably different between $\epsilon = 0.05$ and $\epsilon = 0.10$. However the largest difference between different ϵ is where the change from

6.4. UNEXPLAINED BEHAVIOURS

sign-changing to sign-preserving orbits occur.

For all the measurements where we can estimate the winding number we find a value less than a factor 2 from the one of the theoretically matched orbit. For particle A the ratio between the estimated winding number and the theoretical winding number $\frac{w_{exp}}{w_{theory}}$ is ~ 0.8 . For particle B we find similar with differences varying between 0.8 and 1.2 for measurements 1 and 2 and 0.75 and 1.4 for measurement 3. This suggests that the ϵ values are not exact, but in general the winding numbers are close to what is predicted and thus the matching orbit and ϵ is close to the actual one.

When we look instead at orbits for large $|n_z|$ such as in Figure 5.17 or for $n_z \approx \psi \approx 0$ such as orbit B in Figure 5.16 the orbits for different ϵ, λ and i are all largely the same. The differences in n_z are too small for us to reliably detect. This creates a problem for detecting particles with very small ϵ . For n_z that are very small, we cannot distinguish the orbits for a small ϵ particle with higher ψ orbit for a high ϵ particle with a low ψ orbit. For higher n_z we cannot distinguish straight lines from straight lines. And in the intermediary we are unable to detect a $w > 20$, at best finding a sloping n_z which might just be undesired reversals. Particle A has several orbits that are matched in the intermediary sign-changing n_z region which we can distinguish from $\epsilon = 0$ but we can not estimate the winding number especially well as this measurement is barely half period of the longer period θ_1 .

6.4 Unexplained behaviours

In a number of measurements there are changes in orbit for which we have no explanation. For example in Figure 5.5 the second reversal is completely sharp, the orbit virtually instantly changes, completely 'forgetting' the previous orbit. Why does this occur with the same particle, the same setup, that produce the excellent reversals in Figure 5.1. All conditions we can measure or control are the same and yet the outcome is very different. The only difference is the z coordinate, yet Figure 5.3 was measured at a similar z and showed very few odd behaviours.

6.5 Width compensation

The width compensation discussed in Section 4.3 does solve the issues the previous algorithm had with 'thick' particles for n_z close to 0. It does still produce small errors for $n_z \neq 0$. However it was discovered that Eq 4.4 can be solved explicitly. Given the actual length L of the particle the Euler angle θ can be solved for at each point after a measurement is complete. If this was implemented it would improve the resolution of peaks and allow for more accurate results.

6.6 Goodness of fit

The method for matching the data to a theoretical orbit described in Section 4.6 finds the best fit but it is important to know how good of a fit it is. A flat fitness curve would mean a small change in the data leads to a large change in our matched orbit, i.e we have high uncertainty. To determine the goodness of fit we vary the three fitting parameters ϵ, θ , and i separately and find the best fit for the other two parameters. In Figure 6.1 we find the best matching orbits for Particle A for asymmetries ranging from 0 to 0.2. The plot shows the difference $|n_z - |$ between the theoretical n_z for the best matching orbits for that particular ϵ and the measured n_z peaks for measurement 1 and 2. We see that there is a clear minima around $\epsilon = 0.02$ implying that it is a good fit.

In Figure 6.2 the match of stretch 1 from measurement 1 of particle A is matched to different orbits. We use the best matching asymmetry, match for orbits from the center of the pointcare map to the top. For each orbit we find the best starting position (the initial ψ). The result is a steady slope down to the correct orbit suggesting that this variable also had a clear best value that was chosen.

In Figure 6.3 we use the best matching asymmetry and orbit for stretch 1 from measurement 1 of particle A, and the starting position (initial ψ) is varied over 1 full period. The relatively flat slope suggests that this parameter is not as clearly determined by this fit as the other two parameters.

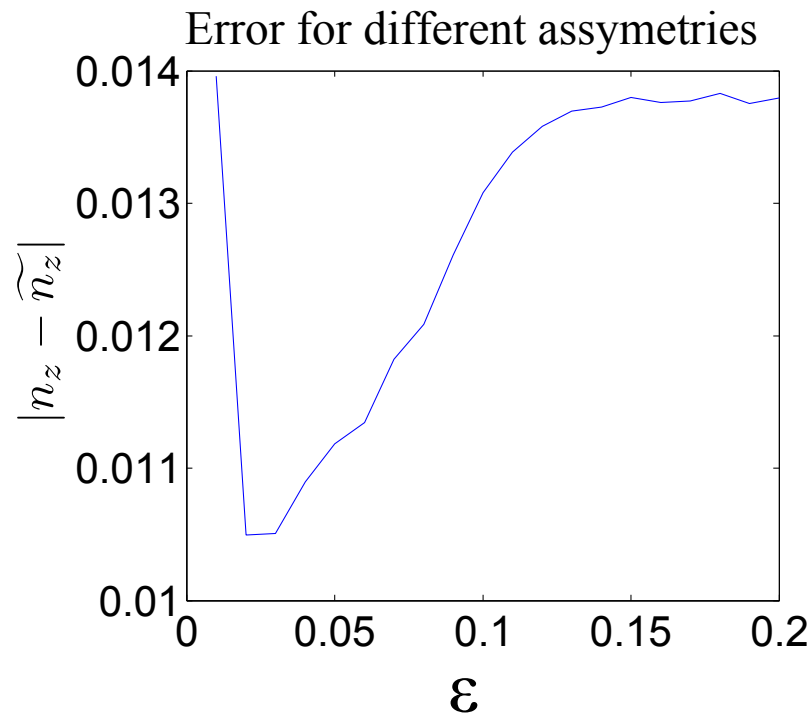


Figure 6.1: We see how the difference between the theoretical n_z and all the measured \widetilde{n}_z for all measurements of particle A for different asymmetries ϵ . For each asymmetry we find the orbit and the initial ψ with the smallest distance for each stretch. We see that there is a clear minima around $\epsilon = 0.02$

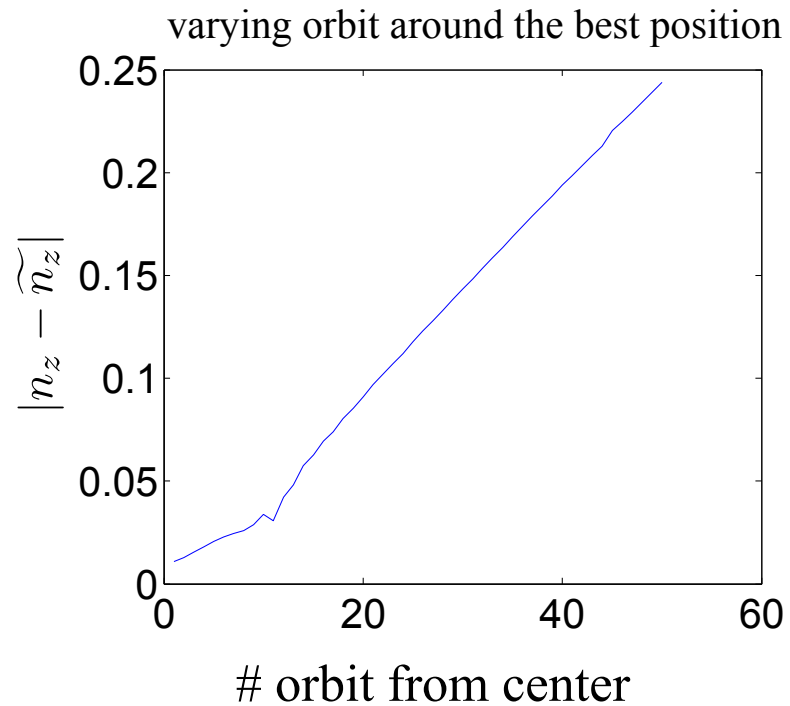


Figure 6.2: The difference between the theoretical n_z and the measured \widetilde{n}_z for the first stretch of the measurement 1 for particle A (seen in Figure 5.1) with the best asymmetry for different orbits. .

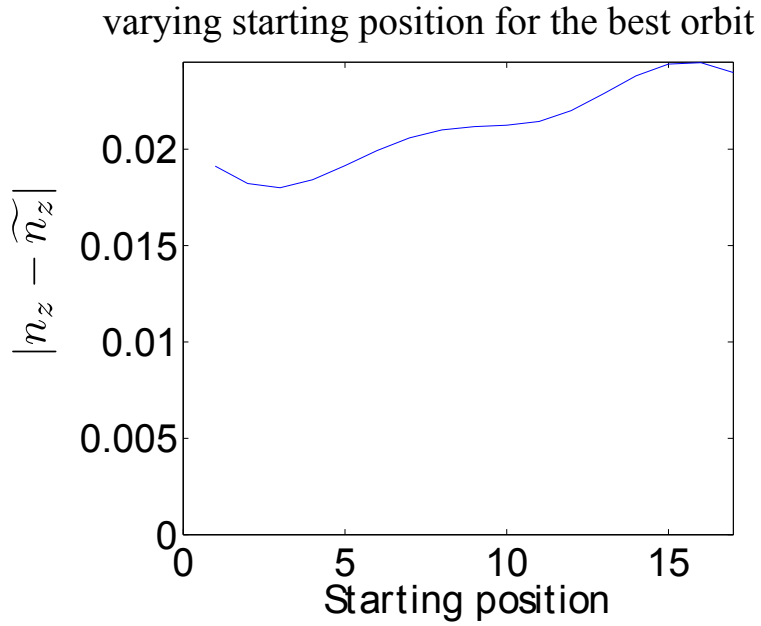


Figure 6.3: The difference between the theoretical n_z and the measured \tilde{n}_z for the first stretch of the first measurement for particle A. The best orbit and best asymmetry are chosen, but different initial conditions are tested. Little variation is shown over different values suggesting that the value found is not strongly matched.

6.7 Automated tracking

The automated tracking discussed in Section 3.3 encountered problems as the experimental setup was changed. When implementing the optical tweezers the particles used were changed from $5\mu\text{m}$ width to $3\mu\text{m}$ width and the objective used was changed to a 60x objective. This meant that the margins to track were made smaller as the particle appears larger in the image.

In order to reduce sinking the speed of the fluid was also increased by a factor 2.5. These two changes together made the tracking unable to reliably track the particle during flow reversals as the simplistic model of constant speed does not hold. A few models for constant acceleration during reversals and variations thereof were implemented but were also unreliable. As such, the automated tracking was not used during the measurements presented in Chapter 5.

Due to the increased flow speed, an automated tracking is also less necessary as measurements

6.7. AUTOMATED TRACKING

take approximately 60% less time. But an automated tracking would still be a significant improvement in saving work time for whoever is doing the measurements. Future efforts could certainly go into finding a better predictive to free up more time to solve other problems instead of manually tracking the particles. If optical tweezers are used that computer controllable and density matching problems are solved, the entire measuring procedure could be automated.

7

Conclusion

The Jeffery orbits are frequently used across scientific fields [5][6] but thus far there has been few experimental studies of the orientational dynamics. In particular the quasi-periodic and chaotic orbits have only been studied experimentally by Einarsson *et al.* [1] and Mishra *et al.* [23]. The goal of the thesis was to verify the theoretical predictions of Yarin *et al.* [11] and Hinch,Leal [10] and to show that the same particle could exhibit quasi-periodic and periodic behaviour for different initial conditions.

There are several measurements that agree well with theoretical models by comparing using both the phase map matching and the winding number estimation. Furthermore, for two particles we have found that different initial conditions exhibit different behaviour, from almost constant to being quasi-periodic with a large regular variation. However we make the assumption that the asymmetry of the broken rods can be compared to that of the triaxial particles without large errors. We can therefore conclude that if this assumption is true, that we have measured the orbits predicted by Yarin *et al.* [11] and Hinch, Leal [10].

We have not found any particles that exhibit chaotic motion. If we again assume that the difference in asymmetry between the broken rods and triaxial particles does not have a major impact, we would not expect to find chaotic orbits for the particles we use. Chaotic orbits are only

common once $\epsilon \geq 0.2$ [3] and the orbits measured match $\epsilon \leq 0.05$.

The time reversibility of the experiment is unreliable. For some measurements the dynamics of the particle revert very well, and for others they does not. We have not understood fully what causes this type of unpredictability that can occur for the same particle only minutes apart. The primary focus of future efforts should be understanding and correcting whatever cause the reversals to be so unreliable. It is possible that the time reversal can be improved by increasing the viscosity of the liquid, or by slowing down reversals. Another possibility is limiting the expansion and contraction of the channel that seems to occur.

The automated tracking was useful in earlier measurements, but with the use of smaller particles, as well as increased flow speed during measurements, a better predictive model is needed to not lose the particle that is tracked during reversals. Automated tracking is also less urgent as measurements take less time. If significantly slower reversals are used to improve time reversibility then the automated tracking will be a higher priority.

Bibliography

- [1] J. Einarsson, et al., Periodic and aperiodic tumbling of microrods advected in a microchannel flow, *Acta Mechanica* (2013) 1–9.
- [2] A. Laas, A study of periodic and quasi-periodic motion of microrods in a shear flow using optical tweezers, Msc thesis, Chalmers University of Technology.
- [3] A. Johansson, Analysis of empirical data on the tumbling of microrods in a shear flow, Master's thesis, Chalmers Univeristy of Technology (2012).
- [4] J. Einarsson, Low reynolds number particle dynamics, Master's thesis, Chalmers Univeristy of Technology.
- [5] T. Kaya, H. Koser, Characterization of hydrodynamic surface interactions of escherichia coli cell bodies in shear flow, *Phys. Rev. Lett.* 103 (2009) 138103.
- [6] E. Cañón-Tapia, M. Chávez-Álvarez, Rotation of uniaxial ellipsoidal particles during simple shear revisited: the influence of elongation ratio, initial distribution of a multiparticle system and amount of shear in the acquisition of a stable orientation, *Journal of Structural Geology* 26 (11) (2004) 2073 – 2087.
URL <http://www.sciencedirect.com/science/article/pii/S0191814104000690>
- [7] A. Einstein, A new determination of molecular dimensions, *Annalen der Physik*.

BIBLIOGRAPHY

- [8] G. B. Jeffery, The motion of ellipsoidal particles immersed in a viscous fluid, Proceedings of the Royal Society A 102.
- [9] P. J. Gierszewski, C. E. Chaffey, Rotation of an isolated triaxial ellipsoid suspended in slow viscous flow, Canadian Journal of Physics 56 (1) (1978) 6–11.
- [10] E. J. Hinch, L. G. Leal, Rotation of small non-axissymmetrical particles in a simple shear flow, J. Fluid Mech 92 (1979) 591–608.
- [11] A. L. Yarin, O. Gottlieb, I. V. Roisman, Chaotic rotation of triaxial ellipsoids in simple shear flow, J. Fluid Mech vol 340 (1997) 83–100.
- [12] F. C. van den Bosch, lecture 1: Surfaces of section, Online material for course.
- [13] H. L. Goldsmith, S. G. Mason, The flow of suspensions through tubes i. single spheres, rods, and discs, Jounrla of colloid science (17).
- [14] O. Harlen, D. Koch, Orientational drift of a fibre suspended in a dilute polymer solution during oscillatory shear flow, J. Non-Newtonian Fluid Mech. 73 (1997) 81–93.
- [15] C. J. S. Petrie, The rheology of fiber suspensions, J. of non-newtonian fluid mechanics 87.
- [16] J. Einarsson, Orientational dynamics of small non-spherical particles in fluid flows, Licentiate thesis, Gothenburg University (2013).
- [17] T. Pedley, Introduction to Fluid Dynamics, Department of Applied Mathematics and Theoretical Physics, University of Cambridge, Silver St., Cambridge CB3 9EW, U.K., 1997.
- [18] S. Childress, An Introduction to Theoretical Fluid Dynamics, Cambridge University Press, 2008, page 117 Starts the discussion of time reversibility of Stokes' Flow.
URL www.math.nyu.edu/faculty/childres/fluidsbook.pdf
- [19] G. K. Bachelor, An Introduction to Fluid Dynamics, Cambridge University Press, 1967, page 212 is definition of Reynolds Number, page 233 is Stokes Law.
- [20] J. Diebel, Representing attitude: Euler angles, unit quaternions, and rotation vectors (2006).

BIBLIOGRAPHY

- [21] J. Munkhammar, Poincare map (2013).
URL mathworld.wolfram.com/PoincareMap.html
- [22] H. G. Schuster, Deterministic Chaos, an introduction, fourth edition Edition.
- [23] Y. N. Mishra, J. Einarsson, et al., A microfluidic device for studies of the orientational dynamics of microrods, Proc. SPIE 8251 2825109.
- [24] B. L. at Stanford, Optical tweezers an introduction.
URL www.stanford.edu/group/blocklab/Optical%20Tweezers%20Introduction.htm
- [25] Fabrication of PDMS microfluidic channels (2010).
URL cismm.cs.unc.edu/wp-content/uploads/2011/03/MicrofluidicsLab.2010.pdf
- [26] Y. Zheng, Poisson equation in a rectangle (2010).
- [27] Nippon Electrical Glass Co, Gap spacers for LCDs: Microrods, www.neg.co.jp/epd/elm/e_prd/other/others_01.pdf.
- [28] J. Canny, A computational approach to edge detection, Pattern Analysis and Machine Intelligence, IEEE Transactions on PAMI-8 (6) (1986) 679–698.
- [29] S. N. Wijewickrema, A. P. Paplinski, C. E. Esson, Reconstruction of spheres using occluding contours from stereo images, in: Pattern Recognition, 2006. ICPR 2006. 18th International Conference on, Vol. 1, IEEE, 2006, pp. 151–154.